FINAL REPORT (3-11)

EMBEDDED COLUMN BASE CONNECTIONS SUBJECTED TO FLEXURE AND AXIAL LOAD: TESTS AND STRENGTH MODELS

DAVID A. GRILLI, AND AMIT M. KANVINDE

DEPARTMENT OF CIVIL AND ENVIRONMENTAL ENGINEERING

UNIVERSITY OF CALIFORNIA, DAVIS, CA 95616

JUNE 8, 2015

EXECUTIVE SUMMARY

Steel column base connections in mid- to high- rise moment frame buildings are often designed by embedding the column into the footing. This enables the development of moment resistance through horizontal bearing stresses against the column flanges. This type of connection, referred to as an Embedded Column Base (ECB) connection, is used when exposed base plate connections (which resist axial force and moment through vertical bearing forces and tension anchors) are unfeasible because they require multiple deeply embedded anchor rods or thick base plates. Moreover, ECB connections may also be used when a stiff or "fixed" base condition is desired. Significant experimental, analytical, and computational research has been conducted on exposed base plate connections, leading to design documents that assist with their design, including the American Institute of Steel Construction's Steel Design Guide One Series, and the Structural Engineers Association of California's Seismic Design Manual. In contrast, research on ECB connections is sparse, with no established guidelines or methods for their design. To address this, this report presents the results of five full scale tests on ECB connections subjected to cyclic lateral deformations in the presence of an axial (tensile or compressive) load. The main variables interrogated include the embedment depth, column size, and the axial load. The experiments demonstrate that ECB connections are able to provide high strength and stiffness, and transfer axial force and moment through a combination of three mechanisms: (1) horizontal bearing stresses acting on the column flanges (2) vertical bearing stresses acting on the embedded base plate at the bottom of the column and (3) panel shear. It was determined that although designed as rotationally fixed, the specimens have some flexibility which must be considered in simulation and design. An assessment of rotational stiffness of ECB connections is provided. A strength model utilizing the observed mechanisms is developed. The model leverages prior research on composite connections, steel coupling beams, and exposed base connections. The strength model is developed to balance the following considerations (1) consistency with physics, and minimal reliance on empirical factors (2) simplicity of application, and (3) agreement with experimental data. The model is able to characterize the observed failure modes as well as experimental strengths with good accuracy. Limitations of the study are discussed along with directions for future work.

INTRODUCTION

Column base connections are critical components in Steel Moment Resisting Frames (SMRFs), transferring axial forces, shear forces and moments from the entire building into the foundation. For low-rise frames (< 3-4 stories), these connections typically include a base plate, which is welded to the bottom of the column and anchored to the footing below with anchor rods – these are typically referred to as "exposed" type connections. As shown in Figure 1a, these connections resist base moments and forces through the development of tension in the anchor rods, along with vertical compressive bearing stresses under the plate. For taller frames, it is often unfeasible to use this mechanism for resisting moments, since it necessitates the use of a large number of deeply embedded anchor rods along with base plates that are extremely thick (e.g. thicker than 75mm). Consequently, structural designers often employ an "embedded" type base connection (see Figure 1b), in which the dominant mechanism of moment resistance is anticipated to be direct bearing between the column and the concrete footing. Significant research has been conducted on the former (i.e., exposed) type of connections, including tests and simulations (Gomez *et al*., 2010; DeWolf & Sarisley, 1980; Thambiratnam & Paramasivam, 1986; Astaneh *et al*., 1992; Fahmy *et al*., 1999; Burda & Itani, 1999; Myers *et al*., 2009), as well as field observations from earthquake damage (Tremblay *et al*., 1995), resulting in methods for strength and stiffness characterization (Gomez *et al*., 2010; Kanvinde *et al*., 2012) and ultimately design guidelines (AISC 341-10, 2010; AISC *Design Guide One* – Fisher and Kloiber, 2006; SEAOC *Seismic Design Manual* SSDM – Grilli and Kanvinde, 2013). However, research on Embedded Column Base (ECB) connections is sparse, and limited to finite element parametric studies (Pertold *et al*., 2000a, b). As a result, the seismic performance of ECB connections is not well understood, with two consequences: (1) there are no established approaches to facilitate

their design, such that AISC *Design Guide One*, and the SEAOC SSDM exclusively address exposed type connections, and (2) there is limited understanding of the stiffness they provide, from the perspective of accurately representing them in simulation and design of the moment frame itself.
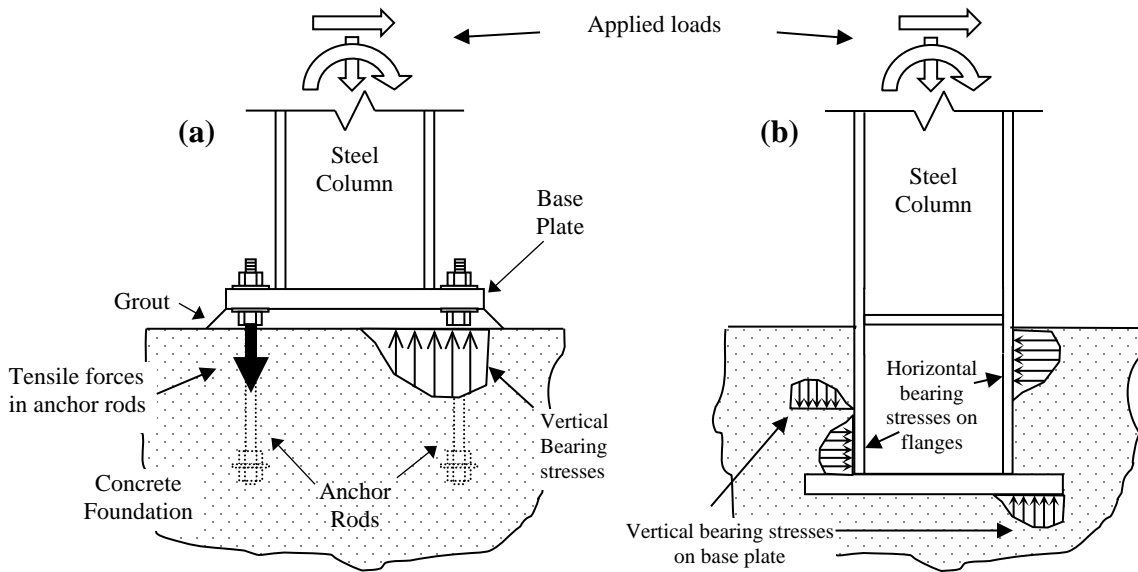
Figure 1 – Column base connections and force transfer mechanisms
(a) exposed type, and (b) embedded type

For the design of ECB connections, practitioners use *ad hoc* methods based on research on other structural components that show mechanisms similar to those expected in ECB connections. Specifically (referring to Figure 1b), these mechanisms include (1) bearing of the joint panel against the concrete, accompanied by shear in the panel zone, and (2) restraint to uplift of the base plate by the concrete above, accompanied by bearing under the toe of the base plate. The latter mechanism is similar to that of exposed connections. The former mechanism, i.e., bearing accompanied by panel zone shear, is well-documented in the ASCE guidelines for composite beam-column connections (ASCE, 1994), and associated research (Deierlein *et al*., 1989; Sheikh

et al., 1989; Cordova and Deierlein, 2005). Moreover, research on steel coupling beams embedded in concrete shear walls also reports on the bearing mechanism to resist moments in the embedded element. This research includes experimental work by Marcakis and Mitchell (1980), Mattock and Gaafar (1981), Shahrooz *et al*. (1993), and Motter (2015).

The latter mechanism (i.e., resistance to uplift of the base plate) has been reported by Morino *et al*. (2003), Cui *et al*. (2009), and more recently, by Barnwell (2015) for shallowly embedded base connections where a floor slab is cast over an exposed type connection. These studies inform physical intuition for each of the mechanisms postulated to be active in the ECB connections. However, applying these for the design/analysis of ECB connections is challenging for three reasons –

1. There are key differences between geometric and statical aspects of the ECB connections, with respect to the mechanisms and specimens examined in the previous studies. For example, the studies on composite connections and coupling beams disregard the effect of column axial force, which is present in ECB column. Moreover, the degree of concrete confinement (in the area of flange bearing) is lower in the coupling beams and beam-column connections, as compared to the ECB connections, which are typically present in wide footings.

2. The ECB connections include interactions of the bearing/panel shear mechanism, along with restrained uplift of the base plate. These interactions occur due to shared stress paths and deformation compatibility between the different mechanisms. Since the various studies have (to a large extent) examined these mechanisms in isolation, understanding their interactions is important for developing strength models.

3. In any of these studies, even for these isolated mechanisms, the stiffness has not been examined. This particularly affects the ECB connections, whose stiffness is critical from the perspective of building performance.

As a result, the *ad hoc* adaptation of these previous studies to ECB connections in the absence of experimental data is susceptible to inaccuracies. Motivated by this, this report presents results from 5 full-scale tests on embedded column base connections. The tests represent typical column base connections for moment-frame buildings, such that their failure is controlled by interactions of flexure and axial load. The primary objective of this report is to present the results of these experiments and to develop seminal knowledge about the seismic response of ECB connections. Specifically, this includes (1) load resistance and failure mechanisms, (2) strength, (3) stiffness, and (4) deformation capacity and dissipation characteristics. Once established, an understanding of these behavioral aspects is used to develop and verify strength models and design approaches for ECB connections. The experiments all feature a wide-flanged steel cantilever column embedded within a concrete footing. Figure 2 shows a schematic illustration of the type of ECB connections used in the test program. All five test specimens are subjected to a cyclic lateral (or flexural) displacement history in the presence of a constant (compressive, tensile, or zero) axial force. The tests investigate the role of various parameters affecting the base connection response, including (1) column size (2) embedment depth, and (3) axial load. These experiments offer: (1) insights into the physics of the connections, including failure modes to inform the development of strength models, and (2) experimental data for validation of the developed models. These insights are leveraged to introduce a strength characterization approach suitable for the design of

ECB connections. The large-scale tests are complemented by ancillary tests for the concrete to effectively interpret results based on measured (rather than specified) material properties.

The report begins by summarizing the current state of practice, and the scope of this investigation. This is followed by an outline of the experimental program, including the test setup, instrumentation, loading protocol, and ancillary tests. The experimental response is discussed in detail, along with a discussion of failure modes, and the associated strength and stiffness. A strength design model is then presented, along with a discussion of limitations of the study and suggested areas of future research.
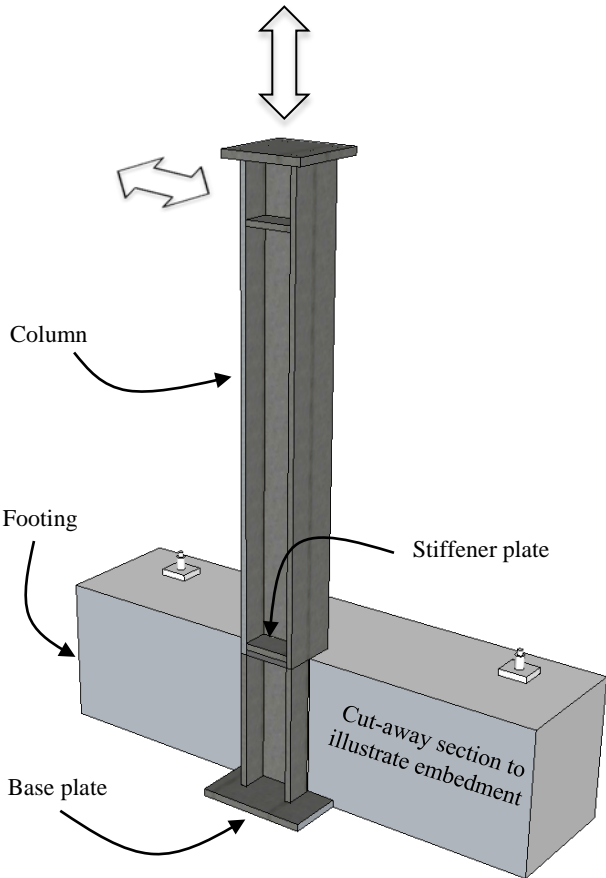

Figure 2 – Schematic illustration of Embedded Column Base
connection used in current study, subjected to axial and lateral loads

To provide context for the experimental program, it is useful to discuss the assumptions and philosophy that underpin the design of ECB connections. The intended yield mechanism in SMRFs involves the formation of plastic hinges at the ends of all beams, and at the column bases (Bruneau *et al.*, 1997). The hinge at the column base may be accommodated in the column itself, or in the base connection. As per current design practice, the former is preferred, assuming that column plastic hinges have greater rotation capacity. The implication is that base connections (including ECB connections) are designed to develop the flexural capacity of the attached column (Grilli and Kanvinde, 2013). As a result, ECB connections may be assumed force–controlled components that are expected to remain predominantly elastic during design level shaking. In the context of this study, this observation motivates an understanding of connection response as it pertains to the onset of nonlinearity or damage, rather than the ultimate strength (which is somewhat secondary). This is especially relevant, since the tested specimens show high deformation capacity and dissipation, much of which is not mobilized within the current design framework.

It is commonly assumed that designing ECB connections to be stronger than the column guarantees sufficient rotational fixity, such that they may be assumed (and simulated as) fixed in frame models and design. Studies by Kanvinde *et al.* (2012) indicate that this is not the case for exposed type connections. Zareian and Kanvinde (2013) noted that overestimating the fixity of base connections (or simulating the base connections as fixed) results in significant detriment to building performance, including increased interstory drift and collapse probability. As a result,

developing an understanding of the fixity provided by the ECB connections is an important motivation for this study.

Embedded Column Base connections may be situated within various types of foundations, including mats, individual pedestals, pedestals connected by grade beams, or pile caps. Types of response and failure modes peculiar to these types of foundations affect the strength and stiffness of ECB connections. In this study, the focus is on response modes in the immediate vicinity of the column embedment, to the extent they can be isolated from those of the surrounding foundation. Finally, the scope of this study is limited to only one connection detail, which is similar to the schematic shown in Figure 2. This detail is distinguished by a base plate attached at the bottom for resisting uplift, and a stiffener plate (similar to a continuity plate) attached at the top of the footing. Other common details feature a large base plate of the top, shear studs attached to column flanges, or supplemental anchor rods on the lower base plate. These variations are not examined, since (1) the study is the first known experimental examination of ECB connections, such that primary consideration is to develop fundamental insights into their response, and (2) the selected detail is highly prevalent in construction practice.

EXPERIMENTAL PROGRAM

All tests specimens were cantilever columns loaded laterally in deformation control as per a cyclic loading protocol. This protocol was applied under a constant axial load (either compressive, tensile, or zero). The major variables interrogated were (1) embedment depth (2) column size, including flange width, and (3) axial load. Table 1 summarizes the test matrix, along with key experimental results (discussed later).

Test Setup

All specimens reflect current construction practice. Figures 3a and b show annotated photographs of the test setup for compressive load (Test #1, 2, 4) and tensile axial load (Test #5) respectively. Test #3, which has no axial load, does not have the fixtures for introduction of axial load, which are present in the other tests. Figure 4 shows a schematic illustration the base connection detail, which is qualitatively similar in all the experiments. The salient features of the test setup and specimens are as follows –

1. All specimens were cantilever columns that extended either z = 2.84m (for Tests #1 and #2 – refer Table 1) or 3.1m (for Tests #3, #4, and #5) above the surface of a concrete pedestal, which measured 3.65m X 1.83m in plan. The height of the cantilever was the location of application of lateral force via a hydraulic actuator. This height is consistent with the inflexion point of a 4.5m first story (assuming it occurs at 2/3rds of the story height), suggesting that the tests may be considered approximately "full-scale" in this aspect. The columns were all A992 Grade 50 (345 MPa), and were designed to remain elastic to force failure in the base connection.

2. As shown in Figures 3a and b, axial load was introduced through a crossbeam and hollow hydraulic jacks attached to the top of the column. To apply axial compression, the hydraulic jacks were positioned as shown in Figure 3a, and were connected to threaded rods which were fixed to concrete blocks fastened to the floor. This loaded the crossbeam downward. To apply axial tension, the cylinders were moved near the middle of the crossbeam and connected to rods that were fixed to the column specimen as shown in Figure 3b. Columns replaced the thread rods on the sides to support the crossbeam. From the perspective of interpretation of the test results, two aspects of the mechanism are relevant: (1) the

mechanism was designed to ensure that the axial load was a "follower force," such that no additional base moment was induced due to the eccentricity of the axial force. For this purpose, clevises (shown in Figures 3a and b) were installed at the elevation of top surface of the concrete footing, and (2) the axial load was held at a constant level throughout the duration of the test.

3. The embedment depth d_{embed} is defined as the distance between the top of the concrete surface, and the top of the embedded base plate. The pedestal dimensions and reinforcement are also illustrated schematically in Figure 4. Referring to the figure, the pedestals were designed with minimal longitudinal and transverse reinforcement such that the observed failure modes and strengths were associated (to the extent possible), with the concrete only. This purpose of this was to facilitate the application of these test results to situations that were significantly dissimilar in terms of reinforcement quantity and layout.

4. The W-section columns were embedded fully through the depth of the block, with plywood cast in between the base of the column and the test floor.

5. Plates were provided at the top and the bottom of the embedment region of the column (see Figure 4). At the bottom, a base plate similar to the ones used in exposed connections was welded to the bottom of the column; dimensions of these plates for each specimen are provided in Table 1. The plate served two purposes. First, it allowed the column to be supported stably as the concrete was poured around it. This is representative of current construction practice, where the column is often supported on a temporary slab. Second, a plate at the bottom is typically prescribed by designers to provide resistance to uplift, i.e., tensile forces in the column. The weld detail between the base plate and column comprised a Partial Joint Penetration (PJP) weld with reinforcing fillet welds. A similar weld detail has

been used previously in base plate tests by Myers *et al.* (2009) and Gomez *et al.* (2010), demonstrating excellent performance. The purpose of these welds was to minimize the likelihood of weld fracture before connection capacity was obtained. To this aim, all welds in the specimen were toughness rated, fabricated using E70 electrode (480 MPa) minimum tensile strength, and the Flux Cored Arc Welding (FCAW) process. At the top of the connection, plates similar to stiffeners were provided between the flanges of the column. The plates were fillet welded (using 12mm welds) along the contact areas on the web and inner flange faces of the column. The main purpose of these plates was to provide resistance to compression in the column; this too is consistent with standard practice. Sometimes, additional plates are added on the exterior of the flanges for this purpose. However, these entail additional fabrication costs, and are often not necessary since axial compression forces in moment frame columns are often low relative to the moments in them.

6. The concrete pedestals were fastened to the laboratory floor using 6 pre-tensioned threaded rods, 3 on each end of the footing. The locations of these rods were chosen to minimize their effect on the stress distribution in the vicinity of the column.
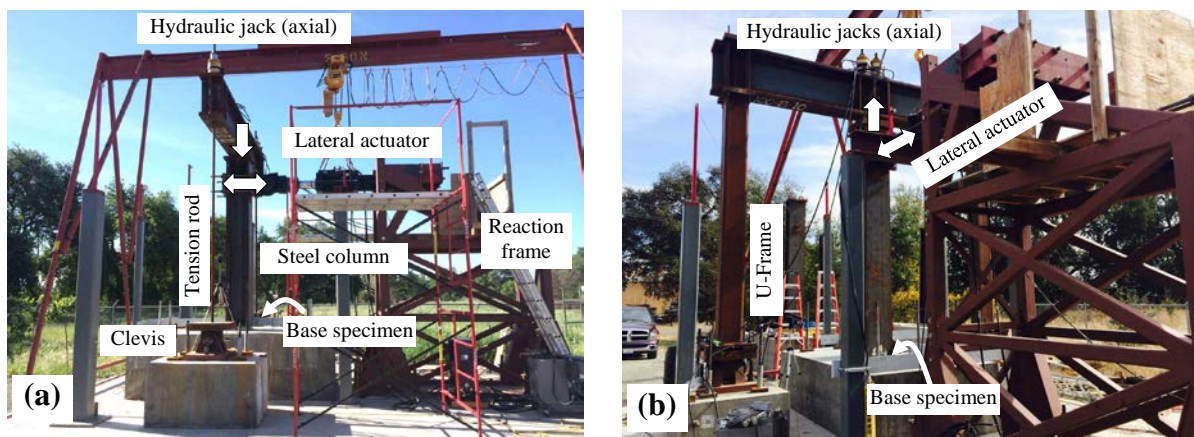
Figure 3 – Test setup (a) for Tests #1, #2, #4 with axial compression, and (b) for Test #5 with axial tension

Standard cylinder tests were performed on samples taken from concrete pours of all pedestals, resulting in an average value of $f_c' = 29.2$ MPa, with a standard deviation of 2.6 MPa.

Compression plate similar to stiffener plate

W14x370 (Test #3,4,5)

840m

d_{embed}

(a)

Lower embedded plate

#3 (10 mm) stirrups (10 hoops) positioned near tie downs. Present in all specimens

W14x370 (Test #1)
W18x311 (Test #2)

584 mm

d_{embed}

508mm

(b)

#6 (19 mm) rebar (4 total)

#5(16 mm) rebar at top and bottom

6 tie downs, 460mm from edge

1.83m

(c)

3.65m

Figure 4 – Schematic illustration of experimental specimens (a) 762mm embedment (b) 508mm embedment (c) plan view; common to both

14

Test Matrix

Table 1 summarizes the test matrix. Referring to the table, the parameters varied include: (1) the embedment depth, (2) axial load, and (3) the column size. The parameter values for each of these were selected based on a consideration of similarity to full-scale connections, as well as of limitations of the test setup; specifically –

1. The columns were sized to ensure failure of the connection. As a result, the sections used in this study are larger than columns that would be embedded in a similar concrete pedestal or grade beam in practice. In turn, the embedment depths are comparable to those commonly used for moment frames.
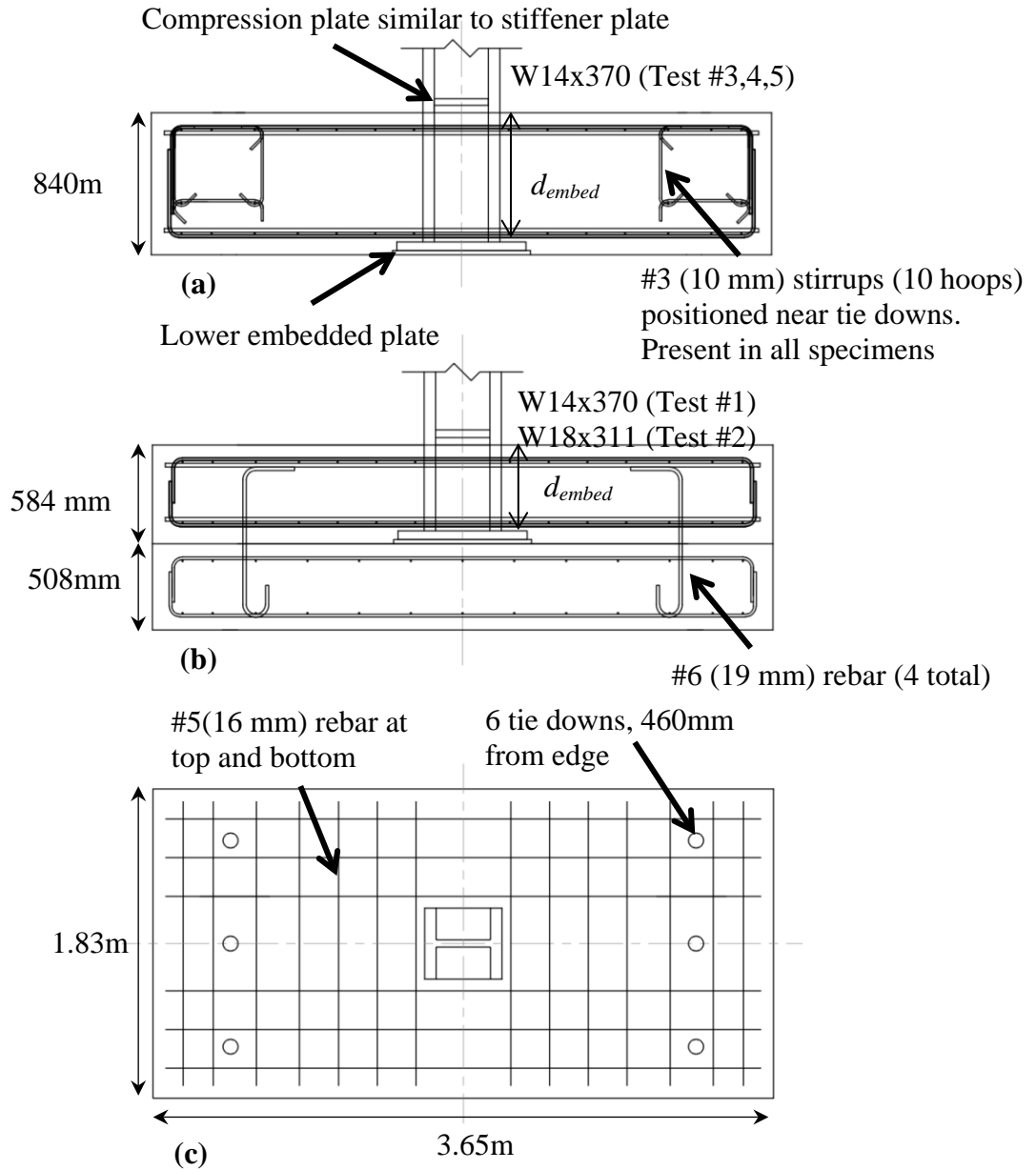
2. The tensile and compressive axial loads were selected to be approximately 10-20% of the yield capacity of a column that would (in a practical setting) have an embedment depth in the range of those used in this study, assuming that the embedment depth is based on ensuring that the connection is stronger than the column in terms of moment capacity. Note that such a hypothetical column is smaller as compared to the ones actually used in the study.

3. The test matrix may be considered fractional factorial, such that pairs (or trios) of tests may be used to examine effects of isolated test variables. For example, Tests #1 and #2 provide a direct examination of the effect of column flange width, whereas Tests #1 and #4 provide a similar interrogation of the effect of embedment.

Loading Protocol

The deformation history applied to the specimens is expressed in terms of column drift ratio (similar to inter-story drift angle), defined as the lateral displacement of the column at the application of the lateral load divided by the distance between the load and the top of the

15

concrete pedestal. For all the tests, displacement-controlled cyclic lateral loading was applied according to the SAC loading protocol (Krawinkler *et al*., 2000) to represent deformation histories consistent with seismic demands in moment frame buildings. Lateral loading was applied quasi-statically, with a loading rate less than 1.8% drift per minute for all phases of testing (i.e. less than 0.018 radian rotation per minute). Referring to Table 1, axial loading was applied to 4 specimens to represent gravity loading and/or tension due to uplift in the column. Axial loads were applied prior to lateral loading and held constant throughout the test. The axial loads shown in Table 1 include a correction for the weight of the axial-load system, as well as the column above the connection area. For tests #1 and 2, the SAC loading protocol was implemented to failure. For Test #3 and 4, drift amplitudes increased incrementally until excessive deformations were achieved. Test #5 was terminated prior to completing the loading protocol due to the slippage of the test block along the test floor and out of plane, and its original positioning could not be recovered. However, significant damage and inelastic deformation in the connection was achieved prior to this slippage.

Instrumentation and measurements

For the purposes of performance assessment and model development, primary streams of data are: (1) lateral displacement at the top of the column and associated actuator force, (2) axial force (3) displacement transducers to measure rocking of the block, and (3) embeddable concrete strain gages in the bearing zone directly ahead of the column flanges, whose purpose was to facilitate characterization of the bearing stress profile in the concrete. Additional transducers were installed to detect out of plane motion of the column as well other unanticipated response. The next section discusses experimental results.

Table 1 – Test matrix and results

Test #	Column Size, (b_f [mm])	p [kN]	d_{embed} [mm]	Base Plate, $t_p \times N \times B$ [mm]	z [m]	M_{base}^{max} [kN-m]	β_{base}^{test} * [10^5 kN-m/rad]	$\dfrac{\Delta_{test}}{\Delta_{fixed}}$ ***	$\dfrac{M_{base}^{y}}{M_{base}^{max}}$	Δ_{max} (%)
1	W14x370 (419)	445 (C)	508	51 × 762 × 762	2.84	2579(+)	3.23	1.21	0.87	3.85
						2613(-)			0.69	3.82
2	W18x311 (305)			51 × 864 × 711		2324(+)	3.84	1.16	0.709	3.01
						2168(-)			0.66	2.89
3	W14x370 (419)	0	762	51 × 762 × 762	3.10	3741(+)	3.07	1.30	0.72	6.97
						3444(-)			0.67	7.77
4		445 (C)				4124 (+)	3.38	1.30	0.66	6.48
						3612(-)			0.81	5.09
5		667 (T)				3800 (+)	3.25	1.29	0.73	2.72**
						3464(-)			0.72	2.65**
							Mean	**1.25**	**0.72**	**4.98**
							CoV	**0.05**	**0.07**	**0.38**

*Average stiffness of both directions
**Test terminated due to slip prior to failure (Mean, COV does not include these data points)
***Notional columns used for Tests #1-5 are W14X145, W14X132, W14X193, W14X211, and W14X193 respectively.

EXPERIMENTAL RESULTS

The discussion of experimental results is presented in four parts. First, the damage progression leading up to failure is described. Second, trends in response with respect to test variables are identified. Third, based on the observed response, a discussion of connection physics and failure modes is presented, with the objective of informing development of strength models. Finally, the stiffness of the connections is critically evaluated, in the context of its anticipated effect on building performance.

Damage progression

Figures 5a-e show the moment-drift plots for all the specimens, whereas Figures 6 and 7 show schematic and photographic illustrations of damage and failure. As discussed previously, where applied, the axial load was introduced at the beginning of the test. The introduction of axial load did not produce any visually observable response in the specimens. Once lateral loading was introduced, all experiments followed a qualitatively similar progression of damage, with some variations. The common aspects of response are described first, before discussing the response peculiar to specific tests.

Figure 6a schematically illustrates damage observed during initial stages of loading (i.e., when the applied drift was less than ≈ 1%). Small cracks (approximately 2mm wide and extending up to 70mm long) began to form near the corners of the column almost immediately after the introduction of lateral load. However, this did not affect the load-deformation response, such that linear elastic response was observed until drifts of 0.005 radians (i.e. 0.5%). Subsequent to this, gradual nonlinearity in the load deformation curve was observed, accompanied by the opening of

a small gap adjacent to the tension flange, accompanied by the growth of the diagonal cracks described previously. This nonlinearity was accompanied by strength degradation as well as pinching response. The pinching response may be attributed to the gapping shown in Figure 6b resulting in relatively unrestrained movement of the column within its "socket," as it moved through the vertical position. Not surprisingly, the extent (i.e., displacement range) of this pinching region increased as the size of the gaps grew to widths exceeding 30mm. The photograph in Figure 7a (taken at the end of Test #3) shows such a gap.

Initial spalling of the concrete ahead of the column flanges was observed at approximately 1% drift. As the loading history progressed beyond this point, the load displacement curve became highly nonlinear. In general, it was observed that the Tests #3-5 with deeper embedment (i.e. d_{embed} = 762mm) showed a more gradual decrease in stiffness, as compared to the more shallowly embedded (d_{embed} = 508mm) specimens. This nonlinearity was accompanied by three types of visible damage (shown in Figures 6b and c for Tests #3-5 at 3-4% drift), which increased in severity (i.e., longer, wider cracks) along with increasing drift –

1. Cracks radiating diagonally outwards from the corners of the column on the top surface of the pedestal (Figures 6a and b), accompanied by slight upward bulging of the concrete in the bearing zone between these cracks. On tension side of the column, significant gapping was observed. This width of this gap was as large as 40mm prior to failure for all experiments (except Test #5) – see Figure 7b.

2. Flexural cracks observed on the sides and the top of the pedestal, on the tension side of the connection (Figure 6b). These cracks were parallel to the flanges of the columns, and were produced by bending of the entire concrete block. These cracks were most prominent in Test

19

#5, which had the tensile axial load, and least prominent in Tests #1, 2, and 4 which had compressive axial load, presumably because the compressive force inhibited the uplift of the block from the strong floor.

3. Diagonal shear cracks on the sides of the block (see Figure 6b), which appeared as straight cracks parallel to the flanges on the top surface.

All these cracks opened and closed as the loading direction was reversed, and they grew in width and length as the applied drift was increased. The damage patterns shown in Figures 6a-c are consistent with drift in one direction, and hence appear unsymmetric, although they are equally pronounced in both directions of loading. In all the tests, the peak moment was achieved between 1.5 and 5% drift. After this, the strength at successive cycle peaks began to deteriorate. This may be attributed to the reduction in the moment resisted by bearing ahead of the flanges as the concrete spalled at the extremities of the bearing block (i.e. at the top and bottom). This process continued until failure of the pedestal (defined as drop in load of at least 30% of the peak load) occurred. In one of the experiments (Test #6), a failure point could not be obtained, owing to irrecoverable slippage of the testing rig. Nevertheless, significant data, including a possible peak load was obtained. In the other tests, one of two scenarios occurred. Shown photographically in Figures 7a and b, these are –

1. In Test #1 and #2, with the shallower embedment (i.e., d_{embed} = 508mm), final failure was accompanied by sudden uplift of a cone of concrete on the tension side of the connection. See photograph in Figure 7a, and schematic illustration in Figure 6c. Referring to the introductory discussion of this report, the base moment is shared by the bearing mechanism, and the restraint to uplift of the base plate at the bottom. As the bearing mechanism becomes

less effective (due to the spalling of concrete, and the associated gapping), a greater fraction of the base moment is resisted by restraining the uplift of the base plate. When the uplift force due to this moment reaches a critical value, failure of the type seen in Figure 7a is observed.

2. For Test #3 and #4 (with the deeper, 762mm embedment), the failure was more gradual, as increasing deformations were accompanied by a steady drop in load. Referring to Table 1, this failure occurs between the drifts of 2.2% and 5% for Tests #3, and 4. The steady drop in load may be attributed to the gradual crushing of concrete ahead of the compression flange (which also result in the gap behind the tension flange), which reduces the effective lever arm of the bearing stress. This results in a pattern of widespread cracking damage (as shown in Figure 7b), rather than the abrupt failure shown in Figure 7a.

In interpreting the discussion above, it is helpful to recall that the columns in the tests were artificially strong (to force connection failure), and hence stiffer as compared to realistically sized columns (which are weaker than the connection). For these hypothetical columns, the elastic cantilever deflections will be larger, resulting in correspondingly greater drifts for each of the observed damage states.
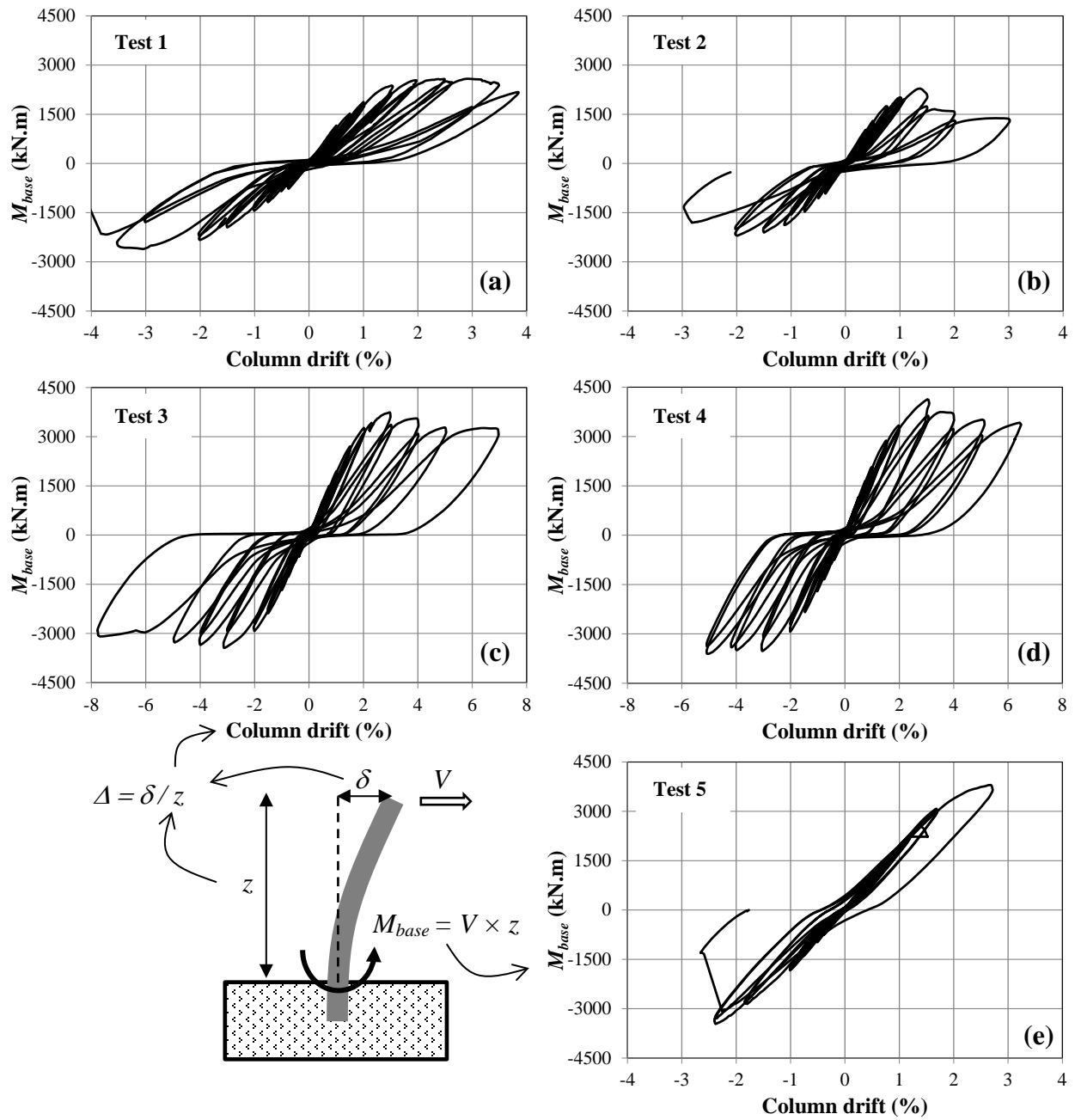
Figure 5 – Moment drift plots for all experiments, and schematic illustration of plotted quantities
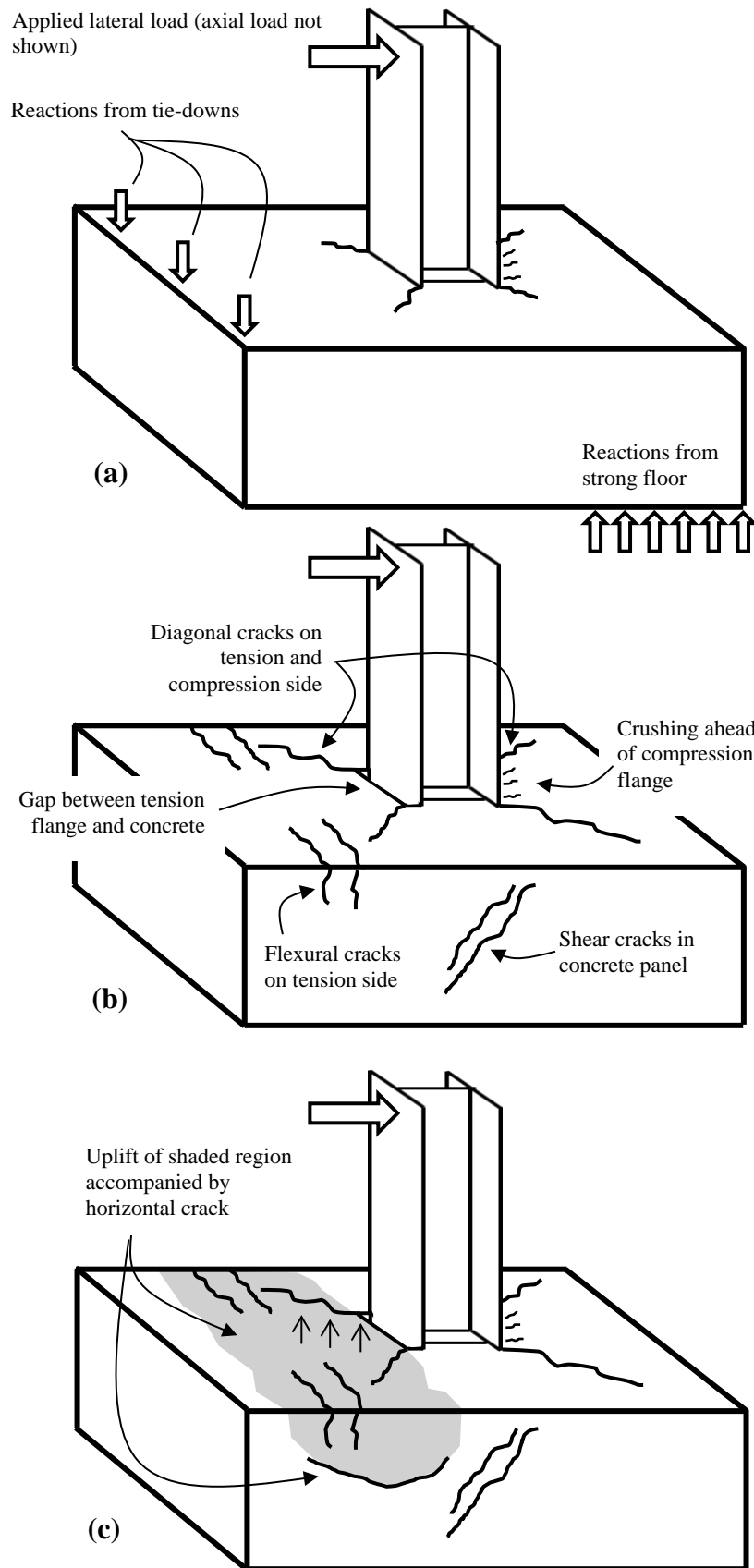
Figure 6 – Typical damage evolution (a) below 1-1.5% drift (b) above 1.5% drift (c) sudden failure mode observed in Tests #1 and #2
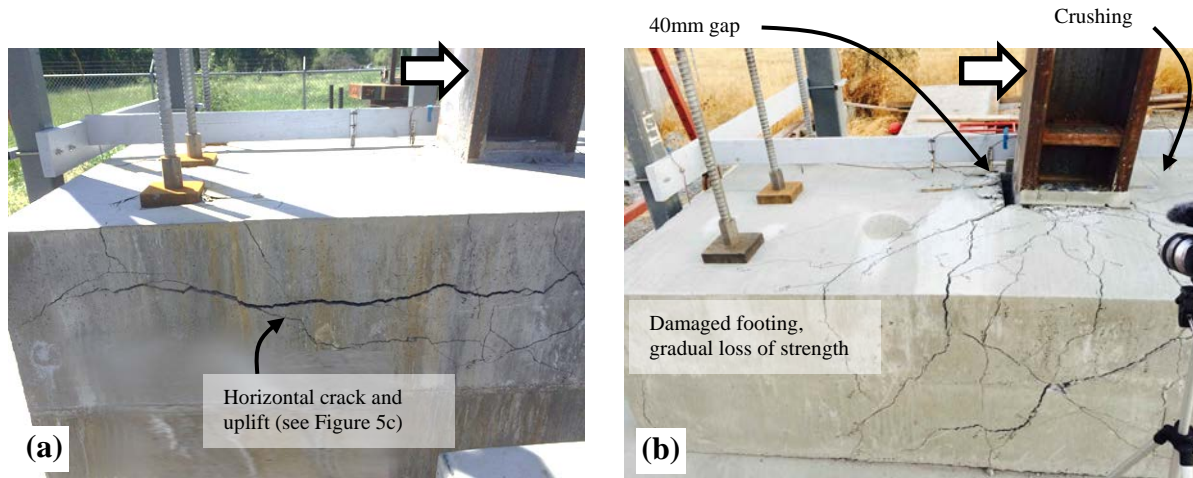
Figure 7 – Observed failure modes (a) Test #2; representative of Tests #1,2 (b) Test #3; representative of Tests #3,4.

Effect of test variables on damage progression

Table 1 summarizes key data measured in the experiments. For each specimen, two strength values are recovered, one corresponding to the maximum moment measured in each direction of loading. These are denoted as M_{base}^{max+} and M_{base}^{max-}, where the positive sign denotes the direction of application of the first deformation cycle. The symbol M_{base}^{max} without the sign is generically used to represent the average of these two values. Specifically, the following observations emerge upon a closer inspection of Table 1, and Figures 5, 6, and 7 –

1. Referring to Table 1, it is immediately apparent that the specimens with deeper embedment have greater strength. Moreover, the ultimate failure mode is different for specimens with the two embedment depths. Specifically, Tests #1 and #2 show a concrete failure cone due to the uplift of the base plate at the bottom of the connection. Tests #3 and #4, have a greater depth of concrete above the base plate, and cannot mobilize this failure mode. Instead, they show

gradual strength deterioration as the effective bearing depth of the column decreases due to spalling/crushing of the concrete at the extremities of the embedded region. Note that even in case of Tests #1 and #2, the strength of the connection is achieved prior to the mobilization of the ultimate failure mode, and is unaffected by it.

2. Most of the experiments are stronger in the positive direction, such that an average value of $M_{base}^{max+} / M_{base}^{max-}$ is 1.08, with a standard deviation of 0.051. This suggests that damage caused by loading in the positive (forward) direction affects the strength in the negative (reverse) direction which is loaded subsequently for each cycle.

3. Comparing Tests #1 and #2 (which are similar in terms of embedment and axial load, but differ in terms of column section and base plate geometry), the 12% higher strength of the specimen in Test #1 may be attributed to the wider flange of the W14 X 370 (420mm), as compared to the flange of the W18X311 (305mm), because the width of the bearing area is proportional to this. Moreover, the moment resisted through the bearing mechanism (relative to the moment resisted through the restraint of base plate uplift) is dependent on the stiffness of the embedded column (a highly flexible column will transfer less moment to the base), and this may be considered another factor in the difference between the observed strengths of Tests #1 and #2.

4. A comparison between Tests #3, #4 and #5 provides a direct assessment of the effect of axial force. Interestingly, application of tensile force (Test #5) appears to have only a modest effect on the flexural strength. On the other hand, the application of a compressive force increases the capacity to a greater degree (comparing Tests #3 and #4).

5. While the peak moment M_{base}^{max} is an important quantity, it is attained after significant inelastic deformation and damage have already occurred. As a result, it may not be suitable

for design of the base connection, especially if it is expected to remain elastic in a "strong-base-weak-column" design framework, which reflects current practice. On the other hand, it is challenging to quantify a "yield" moment, since (1) nonlinear response, albeit modest, is observed even at low moments, and (2) the slope of the backbone curve changes continuously, rather than suddenly, with respect to increasing deformations. Consequently, the term M_{base}^{y} is determined objectively through least-squares fitting of a bilinear curve to the backbone curve obtained from the test, with the condition that the bilinear curve is anchored to the origin, as well as the $(\Delta_{base}^{\max}, M_{base}^{\max})$ point on the backbone curve (which can be determined uniquely), where $\Delta_{base}^{\max}$ represents the drift corresponding to maximum moment. This results in two free parameters, i.e. the "yield" moment M_{base}^{y} and corresponding deformation Δ_{base}^{y}. These quantities are summarized in Table 1 along with other test results. Referring to the values of M_{base}^{y} in the Table, the average value $M_{base}^{y} / M_{base}^{\max}$ is 0.72, suggesting a fraction of the ultimate strength that may be suitable for design. For purposes of convenience, this may be taken as 0.70.

6. All experiments, with the exception of Test #5, achieve deformation capacities in excess of 3% drift (although some strength loss is observed before this deformation). Note that the column for these experiments was disproportionately strong (to induce connection failure); as a result, the elastic deformations of the column were lower than those anticipated for a column in a similar base connection. For reference, the footnotes of Table 1 summarize a notional column that would be consistent with the connection strengths observed in the experiments. In any case, the implication is that the deformation and hysteretic characteristics

of these connections may be considered excellent when evaluated relative to deformation demands in design-level shaking, which are in the range of 2-3% interstory drift.

Connection physics and failure modes

Based on the preceding discussion, and examination of strain gage data (including the embedded strain gages), Figures 8a and b schematically indicate the postulated internal force distribution, and failure modes expected in the type of ECB connections tested in this study. It is assumed that compressive axial force is carried by the top stiffener plate, skin friction along the column, and the bottom base plate. Tensile axial force is carried by skin friction, and downward bearing on the bottom base plate. Referring to Figure 8, the base moment is resisted through a combination of horizontal bearing stresses against the flanges of the column (Figure 8a) and vertical bearing stresses against the lower base plate (Figure 8b). The horizontal bearing stresses are accompanied by shear in the panel zone (similar to panel shear in composite connections – Cordova and Deierlein, 2005). The panel zone consists of the steel web, a compression strut between the flanges of the column, and a compression field (and complementary tension field) in the concrete panel outside the flanges. The tension field is responsible for the diagonal shear cracks observed in Figures 6b and 7b. The column shear is also carried by the horizontal bearing stresses. These physical mechanisms of response may be used to develop strength models for ECB connections. However, for the strength characterization method to be general (such that it may be applied to connections different from the ones tested), consideration of the following issues is critical –

1. *Quantification of failure strength of sub-mechanisms:* Each of the three response mechanisms discussed above (i.e., horizontal bearing, vertical bearing, and joint shear) is

associated with local failure modes (or sub-mechanisms). For example, the vertical bearing mechanism may result in uplift of the concrete (as observed in Tests #1 and #2), or yielding of the lower base plate, or even breakout of the concrete under the compression toe of the base plate if the supporting layer of concrete overlaying the soil is thin. The two latter mechanisms were not observed in the experiments, but they are possible in connections that are sized or designed differently. Similarly, joint shear is controlled by shear yielding of the web, as well as compression strut, and compression field action in the concrete (Cordova and Deierlein, 2005; Sheikh *et al*., 1989). For the horizontal bearing mechanism, concrete crushing is the likely failure mode. Strength checks for each of these mechanisms are necessary in any strength model. Previous research (e.g., Mattock and Gaafar, 1981; Marcakis and Mitchell, 1980 – for coupling beams; Cui *et al*., 2009 – for restrained uplift of base connections; Cordova and Deierlein, 2005) may be suitably used to inform some of these strength checks.

2. *Quantification of interaction between mechanisms:* An understanding of interaction between the various mechanisms is required to develop a successful strength model. Broadly, the interaction is active in two ways. First, the distribution of applied forces (i.e., moment) between the three mechanisms is complex. For example, it may be postulated that the horizontal bearing mechanism is "in series" with joint shear (similar to composite connections – Cordova and Deierlein, 2005), i.e., the forces between these mechanism equilibrate. On the other hand, the horizontal bearing and joint shear mechanisms are "in parallel," such that they are constrained through deformation compatibility, resulting in an indeterminate distribution between the two. A quantitative understanding of these force distributions is necessary to relate strength checks for sub-mechanisms to the overall

28

connection strength. Second, some failure modes may interact due to common stress paths. For example, the concrete that resists uplift of the base plate is also subject to horizontal bearing stresses in the lower region of the column embedment. Thus, it is anticipated that the capacities of the sub-mechanisms may be influenced through interaction with other modes of response.
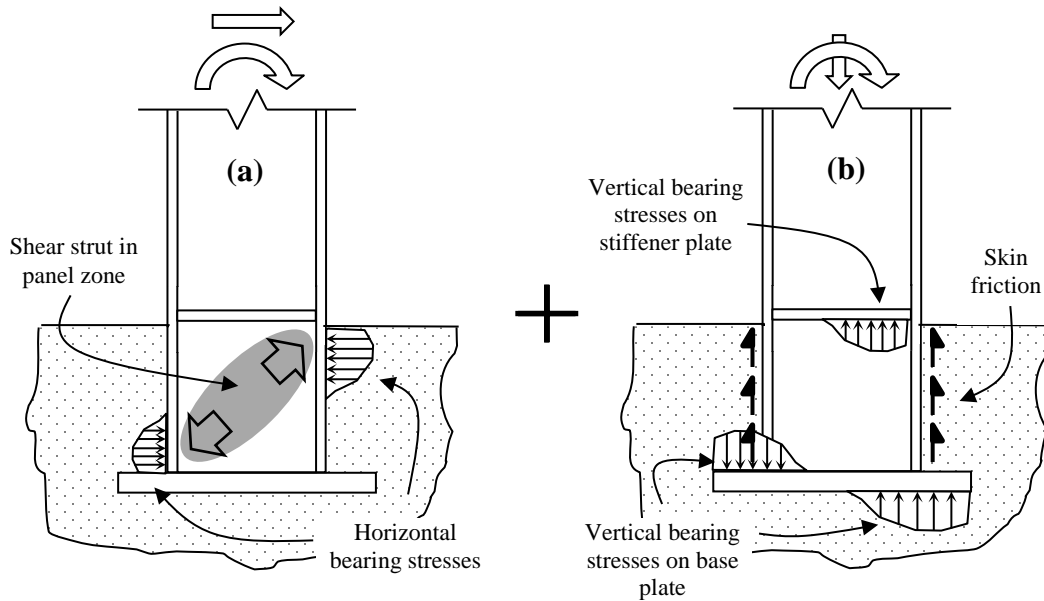
Figure 8 – Load resisting mechanisms (a) horizontal bearing and panel shear accompanied by (b) vertical bearing and skin friction

In summary, a successful strength characterization approach will include: (1) strength checks for failure sub-mechanisms, considering interactions between them, and (2) quantification of force distributions between the response modes, to enable the determination of overall connection strength. Finally, the strength model would address the issue that while the failure modes are associated with ultimate strengths, designing the ECB connection based on ultimate strength will imply significant inelastic action in the connection itself. This is inconsistent with the intent of current design practice (AISC, 2010), in which ECB connections are designed to remain elastic forcing the plastic hinge into the attached column.

Assessment of connection stiffness

Referring to the discussion above, ECB connections designed as per current practice are expected to remain elastic. However, since they are designed based on strength checks, their rotational fixity is not explicitly determined or considered in design of the frame. Characterization of the rotational stiffness of ECB connections is critical from the perspective of ensuring acceptable performance of moment frames. Through parametric simulation, Zareian and Kanvinde (2013) demonstrated that base flexibility has a major effect on various aspects of seismic response, including interstory drift, as well as the shaking intensity associated with collapse. Specifically, simulating the bases as rotationally fixed results in response that is less adverse (i.e., lower interstory drift, high intensity required to trigger collapse) as compared to simulating the bases as flexible. Within this context, this section examines the degree to which the ECB connections tested in this study provide rotational fixity.

An objective evaluation of the rotational fixity is challenging for three reasons. First, referring to Figures 5-e, the base connection response is nonlinear, even in the early stages of loading. Consequently, the initial tangent stiffness is not a suitable representation of the effective stiffness during a design level event. Second, the rotational stiffness of the base interacts with the entire frame to result in response such as interstory drift. As a result, examining the stiffness of the base in isolation is not informative, unless this interaction is considered. Third, since the idealized situation (fixed base) has infinite base stiffness, it is not meaningful to use this as a normalizing (or benchmarking) value for the measured stiffness. To overcome these issues, the following process is established for a convenient, yet meaningful, evaluation of base fixity –

1. For all tests, the moment-drift plots shown in Figures 5a-e are converted to moment-rotation plots for the base connection. The interstory drift angle is converted to the base rotation using the following relationship –

$$\theta_{base} = \theta_{drift} - \frac{M_{base} \times z}{3 \times E_{steel} \times I_{column}} - \theta_{footing} \tag{1}$$

In the above equation, the second and third terms on the right hand side subtract the contributions of (1) the elastic rotation due to flexibility of the column, and (2) rotation due to rocking/uplift of the footing. The latter (determined to be negligible) was measured by vertical displacement transducers attached to the top surface of the footing block, a significant distance away from the zones of damage near the column. Recall that the columns were oversized to force failure in the base, with the implication that the interstory drifts measured in the tests were larger (for it was stiffer than a column that would be sized in practice, which would be weaker than the base). Isolation of the base rotation in this manner enables interpretation of the results in general way, even for columns that are sized differently. Figure 9 illustrates the moment vs base rotation plot generated (for Test #1, positive loading direction) in the manner outlined above. Similar plots are generated for all the experiments.

2. Figure 9 also illustrates the determination of the secant stiffness. As indicated on the figure, the secant stiffness is determined at a base moment corresponding to $M_{base}^y = 0.7 \times M_{base}^{max}$. Referring to prior discussion, this value is consistent with the expected moment in the base, assuming it is designed to remain undamaged as the column develops a plastic hinge. Consequently, the secant stiffness at M_{base}^y is an appropriate parameter for evaluation within a seismic setting. The use of the secant stiffness (at the design level) for connection rotation

is not without precedent; notably used in the context of partially restrained moment connections (Bjorhovde, 1988; ASCE Task Committee, 1998). The secant stiffness, calculated in this manner is denoted β_{base}^{test}, and summarized for all specimens in Table 1.

3. In itself, the value β_{base}^{test} is not meaningful, unless interpreted in the context of its influence on structural response (such as first story drift). However, structural response is a result of indeterminate interactions between the base stiffness and the frame stiffness. To simplify this issue while retaining the key aspects of structural behavior, substructures (such as the one shown in Figure 10) are generated as counterparts to each of the experiments. Each substructure has the following key features –

    a. The column in the substructure is notional, and assigned a stiffness that is consistent with that of a realistically sized column for a given base connection. To achieve this for each test, a W14 section which has moment capacity $M_p \approx M_{base}^y$ is selected, and the corresponding moment of inertia is used in analysis of the substructure. In this way, the biasing effect of the disproportionately strong and stiff column is mitigated.

    b. The rotational spring at the top represents the effective rotational stiffness β_{frame} at the top of the column due to adjacent framing members. This value is determined as per the following equation –

$$\beta_{frame} = \frac{1}{2} \times 2 \times \frac{6 \times E_{steel} \times I_{beam}}{L_{beam}} \qquad (2)$$

In the above equation, I_{beam} and L_{beam} are properties of notional beams framing into the top of the column. The beam sizes are selected based on strong-column weak girder checks with respect to the notional column. The factor "6" on right hand side assumes double curvature bending of the beams, whereas the factor "2" accounts for

the presence of two beams. The factor "1/2" accounts for the fraction of beam stiffness that contributes to the restraint of the lower column, assuming the other half of beam stiffness restrains the upper column. It is acknowledged that these assumptions are approximate, and that true response of the frame may be significantly different from that implied in the above approach for the following reasons: (1) member sizes may deviate from the ones assumed in this study, and (2) frame response may deviate from the idealized response (which assumes beams in double curvature and first mode response). However, the primary objective of this analysis is to provide a general basis for interpreting the measured stiffness of the ECB connections, rather than to precisely estimate story deformations. In this context, the subjectivity introduced by the approximations is acceptable. Sizes of the notional beams and columns (that are consistent with realistic design, given the base connection strength) are summarized in the footnotes of Table 1.

c. If the stiffness β_{frame} is suitably assigned, then the lateral deformation (at the top of the column) for a unit lateral load (i.e., the first story flexibility) may be determined through elastic structural analysis for any value of the base stiffness β_{base}. Two such values are calculated for each experiment. One, termed Δ_{fixed} represents the story drift (or story flexibility) for a fixed base; this is determined by setting $\beta_{base} = \infty$. The second, termed Δ_{test}, is determined by setting $\beta_{base} = \beta_{base}^{test}$. The index $\Delta_{test}/\Delta_{fixed}$ reflects the increase in interstory drift due to flexibility of the base, relative to the fixed base. A value $\Delta_{test}/\Delta_{fixed} = 1$, indicates that the base flexibility does not affect

interstory drift (relative to the fixed base assumption), whereas larger values indicate greater influence. Table 1 summarizes $\Delta_{test}/\Delta_{fixed}$ values for all the experiments.

Referring to the values of $\Delta_{test}/\Delta_{fixed}$, an average value of 1.25 is determined suggesting that the ECB connections are somewhat flexible, such that the first story drift is (on average) 25% larger than that determined through elastic analysis of a fixed base condition. The specimens with the deeper (762mm) embedment have a greater average value of $\Delta_{test}/\Delta_{fixed}$ (1.30 for Tests #3, 4, 5) as compared to Tests #1, 2 with the shallower 508mm embedment, such that average $\Delta_{test}/\Delta_{fixed}$ is 1.19. This is somewhat surprising, since a deeper embedment may be expected to provide higher rotational stiffness. However, this trend may be explained by considering that the embedded base plate also provides significant restraint to rotation since it is restrained by concrete. The observed trend suggests that this stiffness provided by the base plate is large enough, such that reducing the embedment has the effect of lowering the effective bending length of the column beneath the top of the concrete surface. On the other hand, in the specimens with deeper embedments, the additional restraint provided by bearing in the concrete does not offset the increased flexibility due to the greater bending length. In either case, the main implication of the above observations is that ECB connections may not provide a fixed base condition, even when designed to be stronger than the column. However, the 20-30% increase in interstory drifts is relatively modest compared to that generated by the flexibility of exposed type connections (Zareian and Kanvinde, 2013).
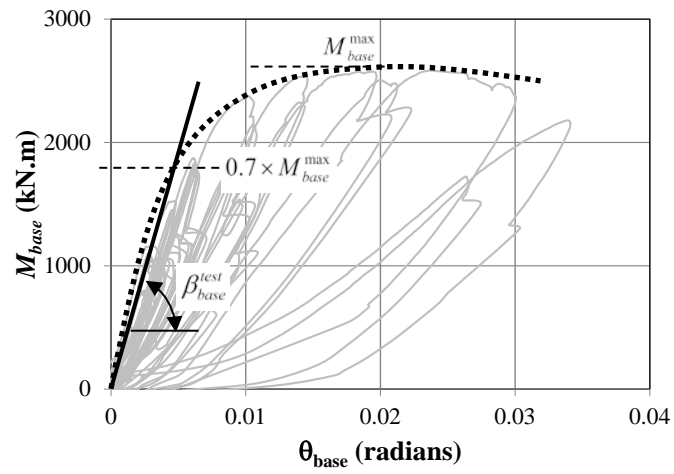
Figure 9 – Schematic illustration of base stiffness calculation, shown for Test #1
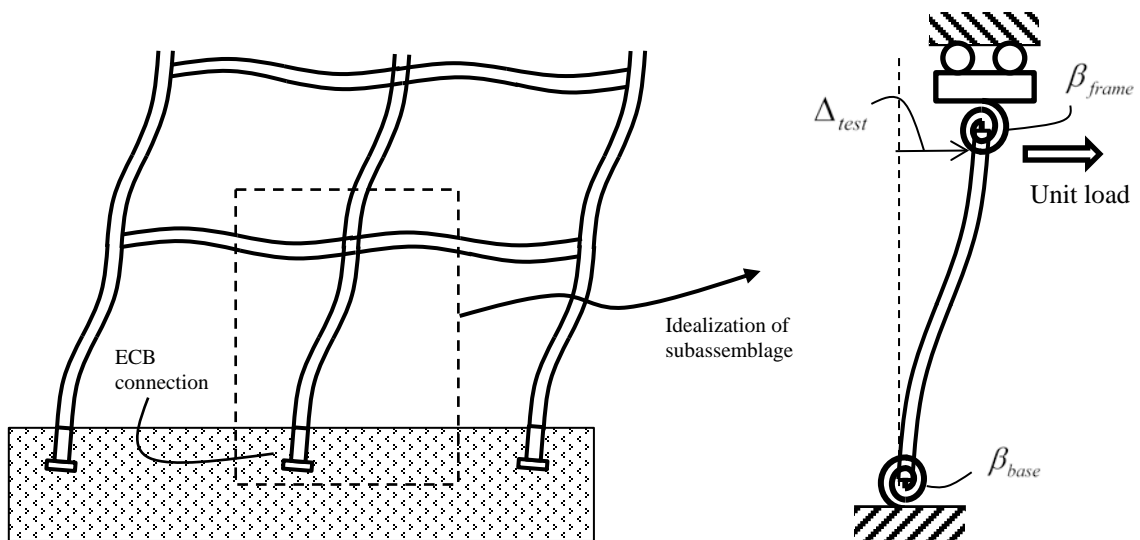
Figure 10 – Subassemblage analysis for benchmarking base stiffness

MODEL FOR STRENGTH CHARACTERIZATION

Based on the observations of the experimental program, this section describes the development of a strength model to facilitate the design of ECB connections. The model is based on two competing considerations (1) to reflect critical aspects of physics and internal force transfer, such that it may be generalized to ECB connections that have not been tested, and (2) to limit cumbersome or complex mathematical expressions or analysis procedures, such that it may be applied conveniently within a practical setting. The model is presented in four parts. First, the problem is rigorously defined to eliminate ambiguity in interpretation of the model. Second, an idealized representation of internal force transfer is presented; this forms the physical basis of the model. Third, strengths for each failure mode (or submechanism) within the connection are discussed, leveraging previous research on similar components. Finally, a scheme is presented for combining these various submechanism strengths into the overall connection strength.

Problem definition

The strength characterization method aims to characterize base moments associated with various limit states (and modes of response), given the ECB geometry and applied axial force (whether axial or tensile), and shear to moment ratio. As a result, the parameters defining the problem may be listed as the column embedment depth d_{embed}, the column section, axial force P, base plate dimensions t_{plate}, B, N, and the shear–to–moment ratio, such that for a given base moment M_{base}, the corresponding column shear V_{column} may be determined as a fraction of it. In addition, the dimensions of the footing as well as material properties of the steel of the base plate F_y^{plate} and the concrete, i.e., f_c' are inputs to the problem.

The problem statement may be defined as follows: (1) given the parameters above, determine the

base moments M_{base}, at which each of the possible limit states is attained, and (2) based on these,

determine the ultimate (or design) moment that can be sustained by the ECB connection. Note

that in the above problem statement (and hence the model formulation), the axial force is

considered a given constant quantity, and the limit states are evaluated with respect to base

moments applied in the presence of this axial force. This implies that the base plate footprint and

thickness, as well as the embedment depth have been selected *a priori* such that failure does not

occur under (tensile or compressive) axial force by itself. This ensures that a finite moment

capacity is available, and recognizes that a design procedure will likely involve preliminary

sizing for one type of force (e.g. axial force), and then iterations to achieve the desired moment

capacity. Methods for sizing the base plate and embedment depth for pure axial load are readily

available in Fisher and Kloiber (2006). Second, this approach reflects the manner of testing,

where the axial force is introduced prior to lateral load. Consequently, the method is based on the

implicit assumption that the strength is insensitive to the order of application of loads.

Idealization of internal force transfer

Figures 11 and 12 schematically illustrate the idealized internal forces associated with force and

moment transfer from the column into the footing. Specifically, Figure 11 shows compressive

axial load transfer, and Figures 12a and b show moment transfer. A corresponding figure for

tensile axial force transfer is not shown, since this is more straightforward to visualize as

compared to that for compressive axial force, because all the tensile force is resisted through

downward bearing stresses on the lower base plate, since the upper stiffener plate is inactive. The

complete force transfer in the connection may be visualized as a superposition of Figures 11,

12a, and 12b. Some of the notation and quantities indicated on the figures will be introduced as the strength method is described in subsequent discussion. The assumed patterns of force transfer, and contributing joint components are based on a combination of (1) experimental observations of failure and strain gage data, (2) quantitative agreement of resulting strength estimates with test data, (3) examination of previous studies on similar components, and (4) continuum finite element simulations that provide insight into internal force transfer. A detailed discussion of these is presented in Grilli (2015). It is acknowledged that these assumed patterns are idealizations of more complicated stress patterns within the connection. Nevertheless, they are necessary from the standpoint of developing an analytical strength model.

Some assumptions inherent to the force distributions shown in Figures 11 and 12, and subsequently used for model development are now summarized –

1. If the axial load is compressive, it is resisted through both the top stiffener plate as well as the bottom base plate. This mechanism is shown in Figure 11. The axial load resisted through the top stiffener plate is distributed through a compression into the footing in a manner that is dependent on the geometry and boundary conditions of the footing. For the test specimens, (and similar configuration) it is assumed that the footprint of this compression field at the elevation of the lower base plate corresponds to the plan dimension of the lower base plate. This is a conservative assumption, since it increases the estimated stresses on the lower base plate. In reality, the compression field (depending on the depth of the footing, and boundary conditions) will be distributed over a larger footprint. Nevertheless it is expedient from the perspective of design development because (1) it provides a convenient way to idealize the vertical stress distribution, especially on the lower plate which resists the applied moment

and axial load through vertical bearing stresses, and (2) the marginal benefit of assuming a more complex stress distribution is low, given that the net axial load in common moment frame columns is low relative to the moment.

2. If the axial force is tensile, it is assumed that it is resisted entirely through downward bearing stresses on the lower base plate, since the upper stiffener plate is not active. In both cases, i.e., tensile or compressive axial load, the contribution of skin friction is ignored because lateral loading results in loss of contact between the column flanges and the concrete, at even low levels of deformation. This mechanism is not illustrated graphically.

3. Referring to Figure 12b which shows an exploded view of the moment transfer, the applied base moment M_{base} is resisted through the column flange forces at the top of the connection, such that $F_{flange}^{top} = M_{base}/h$. A portion of this moment, termed M_{HB} is resisted through horizontal bearing stresses against the joint panel, whereas the remainder (termed M_{VB}) is resisted through vertical bearing stresses on the lower base plate. This implies that the flange forces at the bottom of the flanges are $F_{flange}^{bottom} = M_{VB}/h$, and the vertical shear force on the joint panel is $V_j = F_{flange}^{top} - F_{flange}^{bottom}$. A compression strut induced in the panel zone resists this shear.

4. It is assumed that the effective width of the joint panel $b_j = (b_f + B)/2$, where b_f is the column flange width, and B is the width of the lower base plate. This reflects the development of bearing stresses over a width greater than the column flange, since a portion of the concrete panel outside the flange is mobilized through the development of a compression field. The assumed width of the panel zone affects the joint shear strength, as well as the width over which the horizontal bearing stresses are distributed. In composite

beam column connections, the panel zone width is assumed to consist of an "inner joint," mobilized by face bearing plates in the steel beam (analogous to the top stiffener plate), and an "outer joint," mobilized through compression field action outside the width of the column flanges or face bearing plates. (Deierlein *et al.*, 1989). Unlike composite beam column connections, the ECB connections tested in this study have plates of different width at the top (stiffener plate), and the bottom (lower base plate). The effective joint width is assumed to be the average of these two.

Once the internal force transfer has been established as described above, two additional steps are required before the connection strength can determined. First, the capacities corresponding to the failure modes of force transfer mechanisms illustrated in Figures 12a and b are characterized. Second, these capacities are combined into a net connection moment capacity $M_{base}^{capacity}$, with consideration of (1) the nature of the failure modes (i.e. ductile or brittle), and (2) the evolution of the relative contribution of the different force transfer mechanisms.

$$P$$

Axial force conservatively assumed to transfer to lower plate elevation through compression field, and panel zone compression force

$$f_{VB}^{P} = P/(B \times N)$$
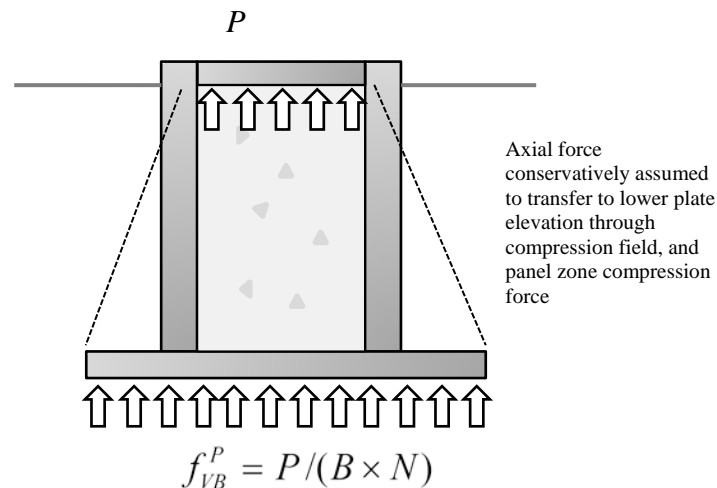
Figure 11 – Idealized force transfer for compressive axial load

M_{base}

V_{column}

(a)

d_U

h

d_L

M_{base}

(b)

V_{column}

F_{flange}^{top}

F_{flange}^{top}

Resultant of bearing block acting at $d_U/2$ from top

V_{column}

Resultant of bearing block acting at $d_L/2$ from bottom

Effective depth of steel web panel in shear

V_j

V_j

$\beta \times \beta_1 \times b_j \times f_c^{'} \times d_U$

$\beta \times \beta_1 \times b_j \times f_c^{'} \times d_L$

Concrete compression strut

F_{flange}^{bottom}

F_{flange}^{bottom}

$f_{VB}^{M} = \dfrac{F_{flange}^{bottom} \times h}{0.21 \times N \times B}$

$0.3 \times N$
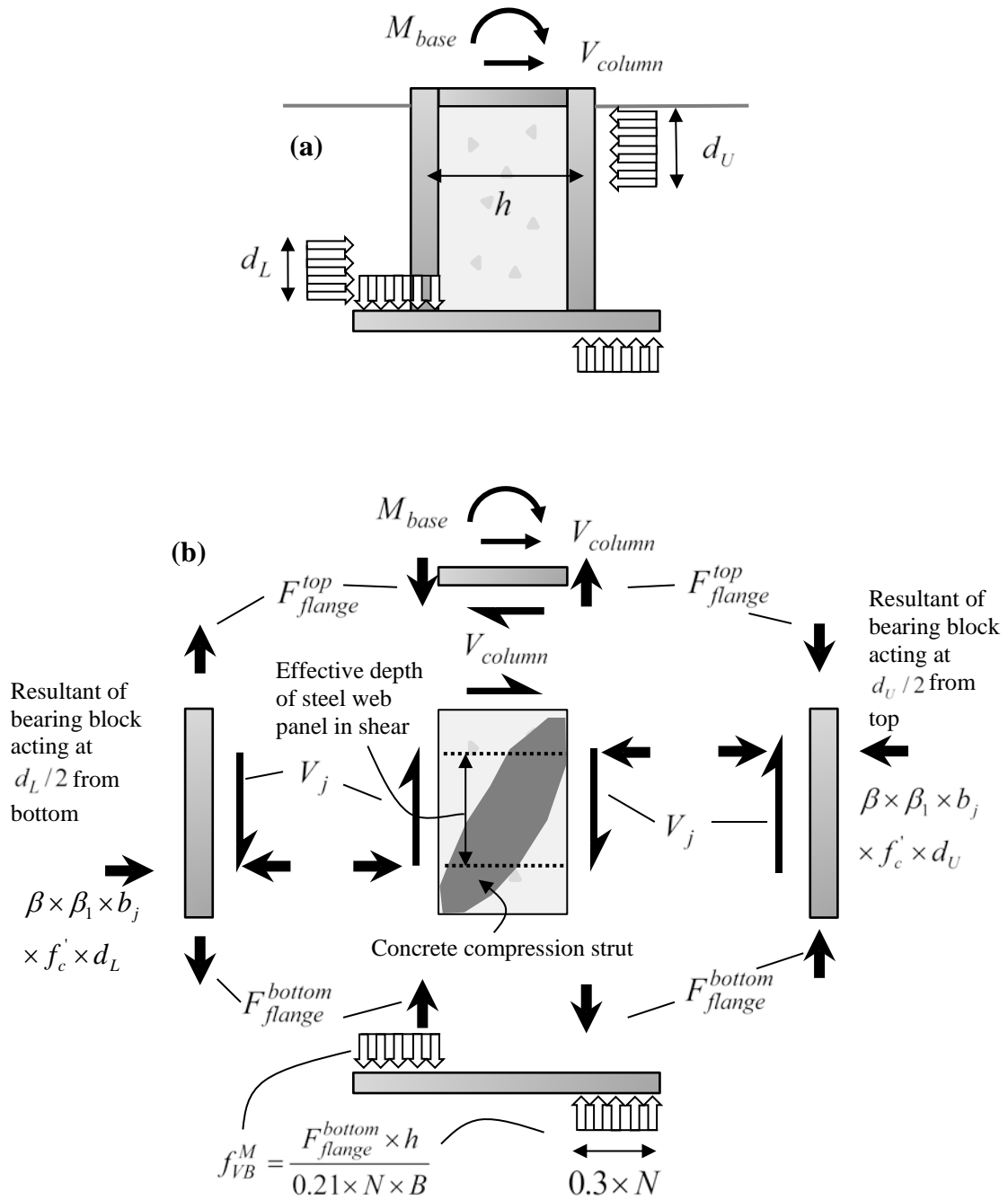
Figure 12 – Idealization of moment transfer (a) overall equilibrium (b) exploded detail

Failure modes and associated moment capacities

Referring to prior discussion, the base moment is resisted due to horizontal and vertical bearing stresses, such that $M_{base} = M_{HB} + M_{VB}$. The resistance due to each of these components is now discussed.

Moment resistance due to horizontal bearing stresses

To characterize the failure modes corresponding to moment transfer through horizontal bearing stresses, it is useful to consider the free body diagram of the panel zone region (see Figure 12b). Referring to this free body diagram, a portion of the applied moment as shown in Equation (3) below is transferred to the panel zone though the joint shear –

$$M_{HB} = M_{base} - M_{VB} = \left(F_{flange}^{top} - F_{flange}^{bottom}\right) \times h = V_j \times h \tag{3}$$

This moment is counteracted by the horizontal bearing stresses in the stress blocks also shown in Figure 12b. A limiting value of M_{HB}, defined as $M_{HB}^{capacity}$ may be determined based on one of two failure modes, i.e., horizontal bearing failure, or joint shear failure.

First, the moment corresponding to bearing failure $M_{HB}^{bearing}$ (which is one possible value of $M_{HB}^{capacity}$) is determined. For this, a trial value of $M_{HB}^{bearing}$ is substituted in force and moment equilibrium equations for the panel zone, which are constructed from the assumed stress blocks (d_U and d_L are the depths of the upper and lower stress blocks respectively, as shown in Figure 12) –

$$V_{column} = \beta \times \beta_1 \times f_c^{'} \times (d_U - d_L) \times b_j \tag{4}$$

and,

$$M_{HB}^{bearing} = \beta \times \beta_1 \times f_c^{'} \times b_j \times \left[d_L \times d_{effective} - \frac{\left(d_L^2 + d_U^2\right)}{2} \right] \quad (5)$$

The above equations rely on three assumptions. First, the bearing stress is assumed equal to $\beta \times \beta_1 \times f_c^{'}$, in which $\beta = 2.0$ simulates the effect of confinement, and the factor $\beta_1 = 0.85$ is used to establish equivalence between a rectangular stress block (implied in the equations above), and the idealized parabolic stress distribution which has a peak stress of $2 \times f_c^{'}$. These factors are consistent with the values used by Mattock and Gaafar (1981), Sheikh *et al.* (1987) and Deierlein *et al.* (1989); and subsequently in the ASCE Guidelines for composite connections (ASCE, 1994). Second, as discussed previously, the width of the joint $b_j = (b_f + B)/2$, to account for the development of the concrete panel outside the flange through the development of a compression field (which is influenced by the reinforcement in this region, and the base and stiffener plates). Third, for the purposes of transferring horizontal forces, the embedment is assumed to be effective only to a limiting value defined as $d_{effective}$. The following expressions (Equations 6 and 7), based on analytical derivations by Hetenyi (1946) are proposed for calculating $d_{effective}$ –

$$d_{effective} = d_{ref} \leq d_{embed}, \text{ where } d_{ref} = \frac{C_0}{\rho_0} \quad (6)$$

$$\rho_0 = \left(\frac{b_f \times \lambda}{4 \times E_{steel} \times I_{column}} \right)^{1/4} \quad (7)$$

In the above equations, C_0 is a constant, whereas the other symbols reflect the stiffness of the steel column, and the stiffness of concrete surrounding the column. Specifically, the term $b_f \times \lambda$ is the resisting stiffness of the concrete per unit length (of the column), such that λ is the spring

stiffness of the concrete per unit area in the horizontal direction. The derivations by Hetenyi (1946) upon which these equations are based derive bearing stresses (as a function of depth) for an end-loaded beam embedded in a semi-infinite elastic medium. These derivations, as well as experimental and computational studies on columns embedded in elastic media such as soil or concrete (Pertold *et al.*, 2000a, b, Hutchinson *et al.*, 2005) indicate that the a large fraction of the moment is resisted by bearing stresses in the vicinity of the free surface, and the bearing stresses attenuate away from this surface. The degree of this attenuation is dependent on the flexural stiffness of the embedded beam relative to the elastic stiffness of the surrounding elastic medium. Hetenyi (1946) demonstrated that the characteristic distance for this attenuation d_{ref} takes the form shown in Equations 6 and 7. As per these equations, a stiff column (relative to the surrounding medium) results in a low value of ρ_0, with the consequence of increasing d_{ref}. On the other hand a flexible column results in a low d_{ref}, indicating that the stresses attenuate rapidly within the stiffer surrounding medium. Referring to equation 6, the depth $d_{effective}$ is equal to d_{ref}, with a maximum possible value d_{embed}, the physical depth of embedment. The classical (Hetenyi, 1946) derivation assumes a canonical semi-infinite half plane within which the column is embedded, without the influence of boundary conditions. The ECB connection is of a finite size in the vertical as well as horizontal directions. Solutions for this situation are not readily available in literature, albeit derivations by Becker and Bevis (2004) suggest a strong influence of boundary conditions in similar problems. As per these derivations, the spring stiffness λ (per unit area) in the horizontal direction is inversely proportional to the bearing width (since it defines an effective gage length for the compression zone) ahead of the flange. In addition, the

stiffness is directly proportional to the modulus of elasticity of the concrete. Accordingly, Equation 7 may be rewritten as follows –

$$\rho_0 = \left(\frac{C_1 \times E_{concrete}}{4 \times E_{steel} \times I_{column}} \right)^{1/4} \qquad (8)$$

Simplifying further, the term d_{ref} may be expressed as –

$$d_{ref} = \frac{C}{\rho}, \text{ where } \rho = \left(\frac{E_{concrete}}{4 \times E_{steel} \times I_{column}} \right)^{1/4} \qquad (9)$$

In the above equation, the factor C, which may be interpreted as a composite factor including the other assumed constants such that $C = C_0 / C_1^{1/4}$ is selected as a calibrated coefficient. This preserves the convenience of the method, while incorporating basic elements of the column-concrete interaction. A value of $C = 1.77$ provides best match with experimental data.

Once $d_{effective}$ is determined as above, the equations 4 and 5 may be solved simultaneously to determine the bearing dimensions d_U and d_L. Following canonical literature on analysis of concrete sections (e.g., McGregor and Wight, 2011), these dimensions are indicators of the strain at the extremity (i.e. top) of the effective embedded zone. As a result, the maximum moment $M_{HB}^{bearing}$ associated with bearing failure corresponds to the bearing dimension d_U and d_L attaining a critical value. Based on experimental data, this critical value is determined to be 60% of the distance between the extremity of the embedment (i.e. the free surface for d_U and the distance $d_{effective}$ for d_L) and the "neutral axis," which is the line that bisects the stress-free region between the two bearing blocks. Figure 13 illustrates this schematically. This approach

for bearing strength (using the 60% value) is similar to that adopted for composite connection design by the ASCE guidelines for composite connections (ASCE, 1994).
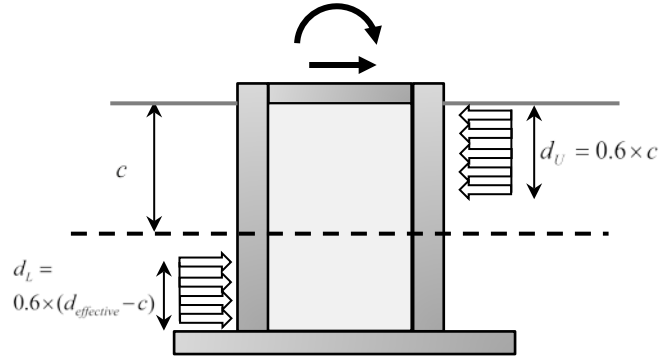
Figure 13 – Critical condition for horizontal bearing failure; in the case shown $d_{effective} = d_{embed}$ (as in the experiments)

Recall that $M_{HB}^{capacity}$ may be controlled by bearing failure or shear failure of the joint panel. The latter may be simply calculated by invoking the relationship between the moment and shear strength, such that –

$$M_{HB}^{shear} = (V_{steel} \times d_w) + (V_{strut,inner} \times h) + (1.25 \times V_{strut,outer} \times h) \tag{10}$$

In the above equation, M_{HB}^{shear} may be calculated as the sum of the moment strengths associated with various components in the panel zone, i.e., the steel web, the concrete strut, and the concrete outer joint. As per the ASCE guidelines for joint shear strength, updated by Cordova and Deierlein (2005), these shear strengths may be determined as –

$$V_{steel} = 0.6 \times F_y^{column} \times t_w \times \left(d_{effective} - \frac{d_U + d_L}{2} \right) \tag{11}$$

$$V_{strut,inner} = 1.7\sqrt{f_c'} \times b_f \times \left(d_{effective} - \frac{d_U + d_L}{2} \right) \leq 0.5 \times f_c' \times b_f \times h, \tag{12}$$

$$V_{strut,outer} = 1.7\sqrt{f_c'} \times b_o \times \left(d_{effective} - \frac{d_U + d_L}{2} \right) \tag{13}$$

The moment capacity due to the horizontal bearing mechanism $M_{HB}^{capacity}$ is then determined as

the minimum of M_{HB}^{shear} and $M_{HB}^{bearing}$. This estimate is retained for use along with the moment

resisted by the entire connection, which also includes the moment resisted due to the vertical

bearing stresses. This is the topic of the next subsection.

Moment resistance due to vertical bearing stresses

Referring to Figure 12, the base plate at the bottom is subjected to bearing stresses on the lower

as well as the upper surfaces, resisting the moment transferred to the base through the column

flanges, as well as the net axial force transferred to the base plate. If the axial force on the

column is compressive, it has two components (1) the portion transferred through the column,

and (2) the remaining axial force transferred into the footing at the top stiffener plate, which is

ultimately transferred to the lower base plate through the compression field in the footing. If the

axial force is tensile, all of it is resisted by downward bearing stresses on the lower base plate. In

either case, the lower base plate is assumed to resist the total axial force (through upward bearing

stresses in the case of compressive axial force, and downward bearing stresses in case of tensile

axial load) in addition to the moment not carried by the horizontal bearing mechanism discussed

in the previous subsection. Referring to Figure 12a, b (which show the moment transfer), this

moment may be expressed as $M_{VB} = F_{flange}^{bottom} \times h$.

The bearing stress distribution due to the axial load and moment is idealized, recognizing that the true stress distribution is a result of a complex interplay between the plate and column flexibility, coupled with the stiffness of the surrounding concrete. The main simplifying assumption is that the bearing stresses may be decomposed into those resisting the moment, and those due to the axial force. For the moment, bearing zones on either end of the base plate may be idealized as rectangular stress blocks with an equal dimension, which is determined (based on agreement with test data, and consistency with the approach used for horizontal bearing) as $d_V = 0.3 \times N$ where N is the length of the lower base plate. Once this is established, the vertical bearing stress in the blocks may be calculated from moment equilibrium as –

$$f_{VB}^M = \frac{M_{VB}}{0.21 \times N \times B} \tag{14}$$

The stress due to the axial force $f_{VB}^P = P/(B \times N)$ considered uniform over the footprint of the base plate may be added to (or subtracted from) the stress blocks determined as per Equation (14) above, resulting in a stepped stress distribution with three zones, as shown in Figure 14. The central zone of width $0.4 \times N$ carries only $f_{VB}^P = P/(B \times N)$, whereas the two outer zones carry the stresses $f_{VB} = f_{VB}^P \pm f_{VB}^M$, since the stresses due to moment may add or subtract from those due to the axial load, depending on the sign of the axial load, and the end zone being considered. Once these stresses are determined, the moment capacity $M_{VB}^{capacity}$ may be controlled by one of four failure modes (which are schematically illustrated in Figures 15a-d)–

1. Bearing failure of the concrete above and/or below the base plate – M_{VB}^b

2. Concrete breakout under the compression toe of the base plate – M_{VB}^c

3. Concrete breakout above the tension side flap of the base plate – M_{VB}^t

4. Yielding of the base plate on the tension or compression side – M_{VB}^{y}

Bearing failure of concrete will occur when the stresses in the stress block reach the bearing strength of concrete (assumed as $f_{VB}^{b} = 1.7 \times f_{c}^{'}$ to account for confinement – see prior discussion for horizontal bearing as well as Fisher and Kloiber, 2006). As a result, M_{VB}^{b} can be conveniently defined as the moment that results in the bearing stress $f_{VB}^{b} = 1.7 \times f_{c}^{'}$ (calculated as per the process above) in the compressive end zone.
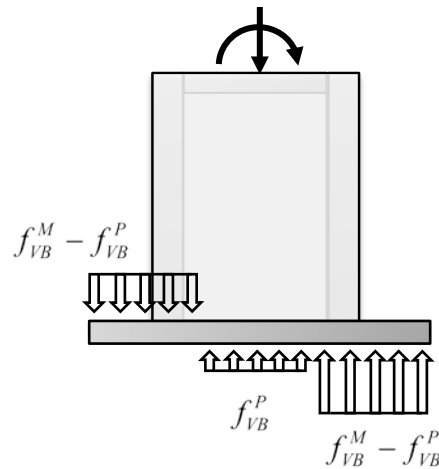
Figure 14 – Stepped bearing distribution due to moment and
axial load at the base plate

As shown in Figures 15b, c the footing in the concrete may also fail due to breakout. This is expected when the embedment is shallow (for tension side breakout – Figure 15c), or if the lower base plate rests on a thin layer of the footing (e.g., a thin slab provided to facilitate erection) supported by the underlying soil (Figure 15b). Recall that the former type of breakout was noted in Tests #1 and #2 of the experimental program. The breakout strength is controlled by the total force in the bearing block, rather than the bearing stress. As a result, the terms M_{VB}^{c} and M_{VB}^{t} are determined by performing a strength check on the total force in the stepped bearing stress

distribution. For tension side breakout, the total bearing force is the force contained in the block (or blocks) that represent the downward stress distribution. For compression side breakout, the total bearing force is the force contained in the block (or blocks) that represent the upward bearing stresses. In either case, the total force may be compared against the capacity for breakout as determined from the equation below –

$$F_{breakout}^{t,c} = \eta \times \frac{40}{9} \times \frac{1}{\sqrt{d_{cover}}} \times \sqrt{f_c'} \times A_{35} \tag{15}$$

The equation above for concrete breakout capacity is based on the Concrete Capacity Design (CCD) method proposed by Fuchs et al., (1995) which has been demonstrated (Gomez et al., 2009) to successfully characterize concrete breakout capacity for various fastenings and concrete embedments. The above equation is especially attractive because it incorporates the "size-effect" in concrete, through the introduction of the square root term $\sqrt{d_{cover}}$, which accounts for the phenomenon (Bažant, 1984) that larger embedments are weaker on a unit basis as compared to smaller embedments. The term A_{35} represents the projected area of a failure cone emanating from the edges of the stress blocks being considered, such that the angle between the cone surface and the horizontal is 35 degrees. Note that depending on the direction of axial force, one or two stress blocks may be active for tension or compression side breakout. In the above equation, d_{cover} is the thickness of the material that must but ruptured for breakout. Thus, for tension side breakout, $d_{cover} = d_{embed}$. The factor η is taken as 1.5 to correct for a discrepancy between the CCD method which assumes that the embedments loaded with a uniform stress. In contrast, the stepped stress distribution on the lower base plate represents a stress gradient, such that the plate rotates (rather than translates) to cause concrete breakout. For the same magnitude of total force, this situation is less intense, and results in a higher capacity. The factor $\eta = 1.5$ is

calibrated to match test data. Alternative models for tension side concrete breakout (e.g., Cui et al. 2009) were examined, but they did not produce reasonable agreement with the experiments. Based on the above process, the moments M_{VB}^t and M_{VB}^c may be determined as moments (applied to the lower base plate) that result in either tension or compression side breakout.

Finally, the bearing stress corresponding to base plate yielding may be determined assuming cantilever bending of the base plate flaps on either side of the column, with yield lines forming parallel to the column flanges. In the following expression (Equation 16), it is implicit that the (1) dimension of the bearing zone is greater than the length of the flap, and (2) the full plastic moment capacity of the base plate is developed in bending. An analogous expression may be derived if this is not the case –

$$f_{VB}^y = \frac{t_{plate}^2 \times F_y^{plate}}{2 \times n^2} \tag{16}$$

In the above equation, n is the length of the flap of the base plate. Once f_{VB}^y is determined in this manner, it may be substituted in Equation (14) to calculate the corresponding moment capacity M_{VB}^y. The minimum of M_{VB}^y, M_{VB}^b, M_{VB}^c, and M_{VB}^t is then taken as $M_{VB}^{capacity}$.

Once the moment capacities $M_{HB}^{capacity}$ and $M_{VB}^{capacity}$ have been determined as per the processes outlined in this subsection, they must be combined to characterize the net connection strength. This is a non-trivial issue owing to several factors, which are discussed in the next section.
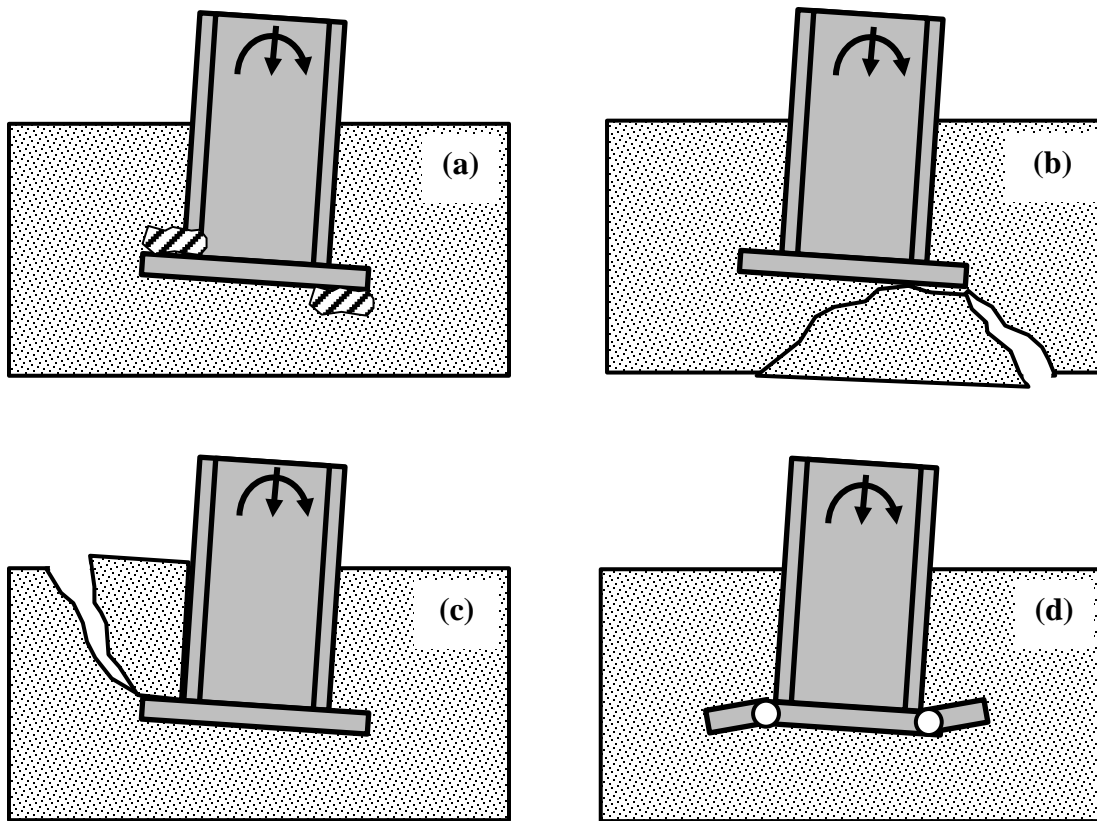
Figure 15 – Failure modes corresponding to vertical bearing moment transfer (a) bearing failure above and below base plate (b) concrete breakout under compression toe (c) concrete breakout above tension flap, and (d) base plate yielding

Combination of moment strengths due to horizontal and vertical bearing

The combination of $M_{HB}^{capacity}$ and $M_{VB}^{capacity}$ to determine a net (or overall) moment capacity for the ECB connection $M_{base}^{capacity}$ is based on a consideration of (1) the evolution of response, and distribution of moments between the horizontal and vertical bearing mechanisms through the loading process, and (2) the interaction between the failure modes. Referring to prior discussion, mechanisms that rely on vertical and horizontal moment transfer are constrained by deformation compatibility, with the implication that they may be considered "in parallel," such that their

moment contributions are additive. However, this also introduces indeterminacy with respect to the relative contributions of these moments. To resolve this, it is assumed that before the moments, M_{HB} or M_{VB} reach their capacities (as determined from the previous section), the net moment M_{base} is distributed in a constant proportion between the two mechanisms, such that –

$$M_{VB} = \alpha \times M_{base} \tag{17}$$

and,

$$M_{HB} = (1-\alpha) \times M_{base} \tag{18}$$

In the above equations, the ratio α controls the relative contribution of the two mechanisms. The contribution of the vertical bearing stresses will diminish as the embedment depth increases, since most of the moment will be carried by the horizontal bearing stresses – refer discussion regarding the effective depth of the embedment. Based on the same discussion, it is implied that the vertical stresses will not resist any moment if the depth exceeds the reference depth of d_{ref} (Equation 6). To reflect this, the following expression is proposed for the ratio α –

$$\alpha = 1 - (d_{embed}/d_{ref}) \geq 0 \tag{19}$$

Given this, various scenarios may be invoked to determine the net moment carried by the connection. The following discussion summarizes each of these scenarios, methods for calculating the associated moment capacity, and the corresponding rationale. Broadly, two situations may be considered (1) failure due to vertical bearing occurs before failure due to horizontal bearing, and (2) failure due to horizontal bearing occurs before failure due to vertical bearing.

Scenario 1 – Failure due to vertical bearing occurs before failure due to horizontal bearing

This scenario occurs if the following inequality is valid –

$$\frac{M_{VB}^{capacity}}{\alpha} \leq \frac{M_{HB}^{capacity}}{1-\alpha} \qquad (20)$$

In this scenario, ultimate strength of the connection may be determined based on the precise mode of failure within the vertical bearing mechanism. As discussed previously, three modes are possible –

1. *Concrete breakout on the tension side:* This type of failure results in a failure plane that interferes with the horizontal bearing mechanism as well, since it is angled upwards towards the free surface. In fact, in two of the specimens tested, i.e. Tests #1 and 2, this type of failure resulted in a sudden loss of capacity of the specimen. As a result, if concrete breakout on the tension side is the controlling mechanism of failure given that vertical bearing failure occurs first, the net moment capacity of the connection may be simply determined as the moment carried by the connection at the instant when the vertical bearing mechanism reaches its failure mode, i.e., -

$$M_{base}^{capacity} = M_{VB}^{t}/\alpha \qquad (21)$$

2. *Concrete breakout on the compression side:* Failure of this type results in the loss of moment carrying capacity due to vertical bearing, but because the failure plane is below the lower base plate (and therefore does not interfere with the horizontal bearing mechanism), the horizontal bearing capacity is still retained. Accordingly, if the critical value of M_{VB} is controlled by breakout on the compression side, the moment capacity of the base may be characterized as –

$$M_{base}^{capacity} = M_{HB}^{capacity} \qquad (22)$$

54

3. Concrete crushing or base plate yielding: Both of these are ductile failure modes and may be assumed continue to carry moment until the horizontal bearing capacity is reached (although this has not been verified in the experiments – which showed other failure modes). As a result, if any of these control M_{VB}, the connection strength may be estimated as per Equation (23) below –

$$M_{base}^{capacity} = M_{HB}^{capacity} + M_{VB}^{b} \text{ or } M_{base}^{capacity} = M_{HB}^{capacity} + M_{VB}^{t} \tag{23}$$

Scenario 2 – Failure due to horizontal bearing occurs before failure due to vertical bearing

This occurs if the following inequality is valid –

$$\frac{M_{VB}^{capacity}}{\alpha} > \frac{M_{HB}^{capacity}}{1-\alpha} \tag{24}$$

As discussed previously, $M_{HB}^{capacity}$ may be controlled by bearing failure or joint shear failure. Each of these cases is now considered separately. If bearing failure controls, then $M_{HB}^{capacity} = M_{HB}^{bearing}$, and the moment carried by the horizontal bearing stresses degrades gradually with increasing deformations. This is because spalling of the concrete at the extremities of the bearing zone reduces the effective depth of bearing. This type of behavior is observed in all tests (note the post-peak response in Figure 5). This type of response cannot be described as sudden or brittle, and moreover it does not appear to reduce the effectiveness of the vertical bearing mechanism. However, since horizontal bearing failure decreases the moment M_{HB}, it is expected that (1) the ratio α defining the moment distribution between the two mechanisms is no longer valid, and (2) the vertical bearing mechanism will now carry a larger proportion of the moment. The implication is that as deformations increase beyond those required to initiate horizontal bearing failure, the moment carried by horizontal bearing will reduce, accompanied by a

corresponding increase in the moment carried by vertical bearing. Ultimate failure will occur when one of the failure modes in vertical bearing is triggered. This type of response is shown by Tests #1 and #2 where the tension-side breakout (a vertical bearing failure mode) is triggered at large deformations after significant reduction in the moment carried by horizontal bearing. To reflect this response, the maximum moment carried by the connection may be determined as –

$$M_{base}^{capacity} = \max\left(\kappa \times M_{HB}^{capacity} + M_{VB}^{capacity}, \frac{M_{HB}^{capacity}}{1-\alpha} \right) \tag{25}$$

The right hand side of the above equation contains two candidates for the moment capacity associated with this failure mode, to reflect two possible scenarios, which are –

1. The decrease in M_{HB} (after $M_{HB}^{capacity}$ is reached) is greater than the corresponding increase in M_{VB} before failure is achieved in the vertical bearing mode. In this case, the peak moment sustained by the connection is simply $M_{HB}^{capacity}$. This is the case as observed in Tests # 1 and #2.

2. The decrease in M_{HB} (after $M_{HB}^{capacity}$ is reached) is lower relative to the increase in M_{VB}, before it reaches failure. This is possible, for example, in shallowly embedded bases (not tested in the current study) where horizontal bearing provides only modest moment resistance (which is reached quickly), followed by a period during which the vertical bearing stresses are mobilized, to achieve a moment strength higher than $M_{HB}^{capacity}$. In this case, the peak moment sustained by the connection is the sum of $M_{VB}^{capacity}$ and the reduced moment $\kappa \times M_{HB}^{capacity}$ carried by the horizontal bearing mechanism at the instant of failure in the vertical bearing mechanism.

The factor κ (which can have a maximum value of 1.0) reflects the reduction of M_{HB}, and is physically dependent on the magnitude of deformations applied after $M_{HB}^{capacity}$ has been achieved. Characterization of κ based on deformations is challenging for several reasons, primarily because the strength method is based on assumed stress distributions, rather than deformation fields. As a result, the following relationship is proposed to determine the factor κ -

$$\kappa = \left(\frac{M_{VB}^{capacity} \times (1-\alpha)}{M_{HB}^{capacity} \times \alpha} \right)^{-2} \tag{26}$$

In the above equation, the quantity $\dfrac{M_{VB}^{capacity} \times (1-\alpha)}{M_{HB}^{capacity} \times \alpha}$ reflects a normalized index of the residual (or available) capacity in the vertical bearing mechanism at the instant when the horizontal bearing strength is reached. For example, if $\dfrac{M_{VB}^{capacity} \times (1-\alpha)}{M_{HB}^{capacity} \times \alpha} = 1$, then the implication is that the vertical and horizontal bearing failures are reached simultaneously. As a result, $\kappa = 1$, because no additional deformations can be applied to the connection after $M_{HB}^{capacity}$ capacity has been reached (since $M_{VB}^{capacity}$ is also simultaneously reached). On the other hand, if $\dfrac{M_{VB}^{capacity} \times (1-\alpha)}{M_{HB}^{capacity} \times \alpha} > 1$, then the implication is that additional deformations may be applied before $M_{VB}^{capacity}$ is reached, and these deformations will be accompanied by a reduction in M_{HB}. The relationship in Equation 26 above reflects this assumed response, and is calibrated to match test data, especially the breakout failure strengths observed for Tests # 1 and #2.

If shear failure controls, in which case $M_{HB}^{capacity} = M_{HB}^{shear}$, then the failure is brittle, with no possibility of additional moment being sustained in any of the failure modes. In this case, the moment capacity of the connection may be calculated through Equation (27) below –

57

$$M_{base}^{capacity} = M_{HB}^{shear} / (1 - \alpha) \qquad (27)$$

In the above equation, $M_{base}^{capacity}$ is the moment carried in the connection when the horizontal bearing mechanism reaches its capacity. The above equation is similar to Equation 21 presented previously for the brittle failure mode (i.e., tension breakout) in the vertical bearing mechanism.

The flowchart shown in Figure 16 schematically illustrates the process described above to determine base connection capacity $M_{base}^{capacity}$. Referring to the Figure, it is evident that the algorithm is suited for automated implementation using a computer program, given its complexity. To design the base (i.e., to solve the inverse problem), the computer program may be executed with various trial parameters (such as embedment, plate thickness etc.) until an acceptable solution is determined within the design constraints. A note of caution here is that the strength determined as per the method above is consistent with the ultimate strength of the connection, with the implication that if designed based on this strength, the connection will sustain inelastic deformations during design level shaking. As discussed previously, the average ratio $M_{base}^{y} / M_{base}^{max} = 0.70$ may be considered a suitable fraction of the ultimate strength for design purposes, since it limits inelastic deformations. Given the nonlinearity of the load-deformation curve (and the processes responsible for it, e.g., progressive bearing failure ahead of the column flange) is gradual, it is challenging to identify a precise physical event and a corresponding first yield moment for the connection. Consequently, designing the connection for a fraction of the ultimate strength is an expedient strategy. The next section evaluates the efficacy of the proposed method (i.e., the determined strengths as well as the implied response) against the test data.

Given quantities:

- P, d_{embed}, f_c',
- Column size
- Base plate dimensions

Determine $d_{effective}$ and α using Equations 6, 9 and 19

Iteration loop

Increment M and V

Compute M_{VB}^{b}, M_{VB}^{c}, M_{VB}^{t}, M_{VB}^{y} using Equations 14-16. Set
$M_{VB}^{capacity} = \min\{M_{VB}^{b}, M_{VB}^{c}, M_{VB}^{t}, M_{VB}^{y}\}$

Compute d_U, d_L, $M_{HB}^{bearing}$, M_{HB}^{shear}, using Equations 4, 5, 10-13

Determine failure scenario (Eq 20, 24)

Scenario 1, Eq 20 is true

Scenario 2, Eq 24 is true

No

$d_U < (0.6 \times c)$

$M_{HB}^{capacity} = M_{HB}^{bearing}$

Yes

$M_{VB}^{capacity} = M_{VB}^{c}$?

Yes

No

No

$M_{HB}^{bearing} < M_{HB}^{shear}$

Yes

$M_{base}^{capacity} = M_{HB}^{bearing}$

$M_{base}^{capacity} = \min\begin{Bmatrix} M_{VB}^{t}/\alpha \\ M_{VB}^{b,y} + M_{HB}^{capacity} \end{Bmatrix}$

$M_{HB}^{capacity} = M_{HB}^{shear}$

$M_{base}^{capacity} = M_{HB}^{shear}/(1-\alpha)$

$M_{HB}^{capacity} = M_{HB}^{bearing}$?

No

Yes

$M_{base}^{capacity} = \max\begin{Bmatrix} \kappa M_{HB}^{bearing} + M_{VB}^{capacity} \\ M_{HB}^{bearing}/(1-\alpha) \end{Bmatrix}$
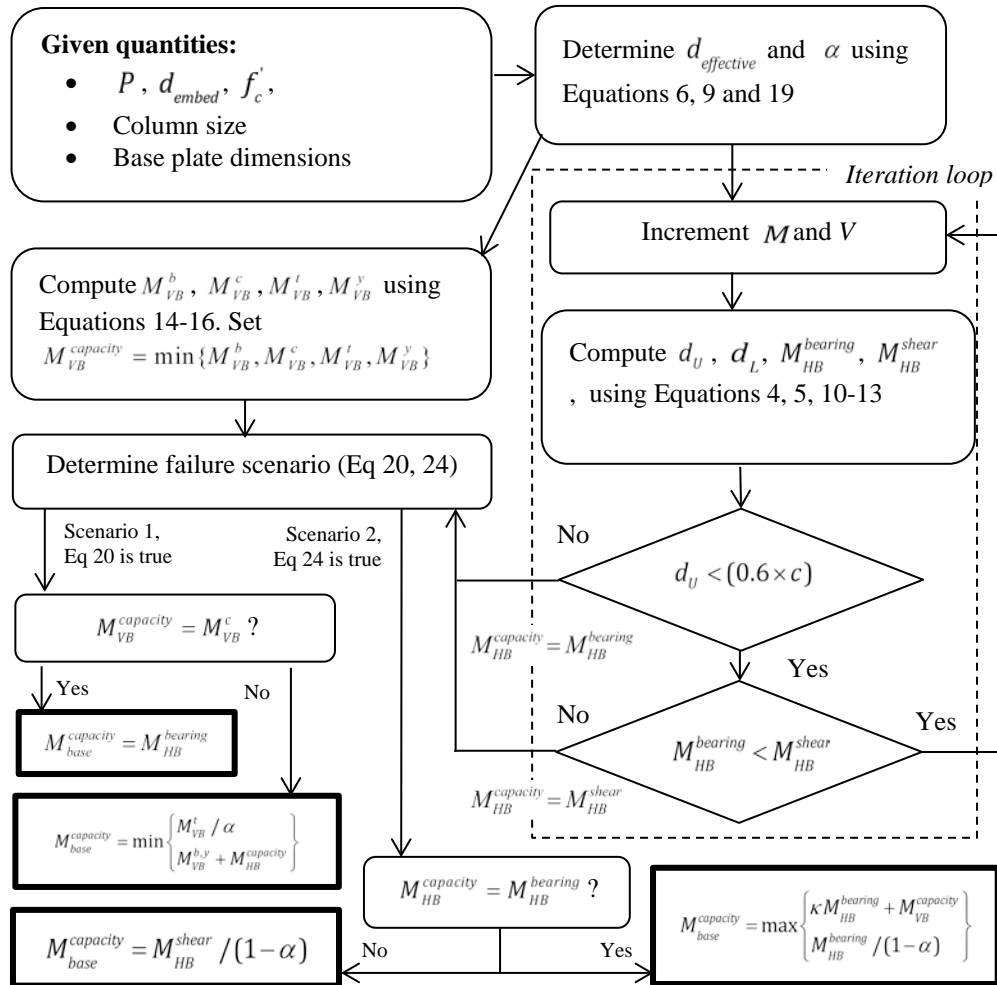
Figure 16 – Flowchart illustrating strength characterization process; dark borders indicate final estimates.

ASSESSMENT OF STRENGTH MODEL RELATIVE TO TEST DATA

Figure 17a-e show the strength estimate $M_{base}^{capacity}$, determined as per the method presented in the previous section, overlaid on the moment-drift curves for all the five specimens. The figure graphically indicates that the agreement between the predicted and observed moment strength is excellent for all the five experiments. Table 2 summarizes these observations quantitatively. The key observations from the Table and Figures 17a-e are –

1. The Table shows test-predicted ratios for both directions of loading for each test. On average, the test-predicted ratio is 1.01 (with a standard deviation of 0.06), which may be interpreted to indicate that the model appears to characterize the strength of the base connections with accuracy.

2. The Table includes the maximum experimental moments M_{max} determined from both directions of loading in the cyclic tests. The value for the direction loaded first (denoted forward) is listed first is followed by the reverse direction. The strength in the forward direction is on average 1.08 times stronger as compared to the strength in the reverse direction. This trend is also reflected in the test-predicted ratios such that the average test-predicted ratio for the forward direction is 1.03, whereas for the reverse direction, it is 0.95. The model cannot account for strength degradation due to loading in the opposite direction, which is the reason for this bias.

3. In three of the tests, (i.e., Test #3, #4 and #5 with d_{embed} = 762mm), the peak strength (as determined by the method) was controlled by horizontal bearing, such that $M_{base}^{capacity} = M_{HB}^{capacity} /(1-\alpha)$. The observed physical response was consistent with this, such that a loss in moment capacity was observed after reaching a peak strength, which was

accompanied by spalling of concrete in the bearing region directly ahead of the column flange.

4. The capacity of Test #1 (with d_{embed} = 508mm) was controlled by bearing as well. However, after reaching the peak strength (accompanied by concrete spalling as in Tests #3, #4, and #5), the moment capacity gradually diminished until sudden failure occurred due to concrete breakout on the tension side of the connection. The moment corresponding to this breakout event (which occurs only on one side of the specimen, after which the test is terminated) represents the base moment $\kappa \times M_{HB}^{capacity} + M_{VB}^{t}$ (refer Equation 25). However, since it is lower than $M_{base}^{capacity} = M_{HB}^{capacity} /(1-\alpha)$, it does not control the strength of the connection. Nevertheless, the agreement of the measured value of this moment M_{base} = 2177 kN.m (as shown in Figure 17a) relative to its analytical counterpart $\kappa \times M_{HB}^{capacity} + M_{VB}^{t}$ = 2337 kN.m provides additional physical validation of the proposed method.

5. The strength of Test #2 is also ultimately controlled by Equation 25 such that $M_{base}^{capacity} = M_{HB}^{capacity} /(1-\alpha)$. However, as with Test #1, strength degradation and breakout occurred subsequent to reaching $M_{base}^{capacity}$. The measured value of this moment was M_{base} = 1807 kN.m, and its analytical counterpart is $\kappa \times M_{HB}^{capacity} + M_{VB}^{t}$ = 2083 kN.m, with $\kappa = 0.59$.

In summary, the connection strengths determined by the method are generally in good agreement with the experimental values. The test-to-predicted ratios do not appear to show significant bias with respect to any of the test variables. Moreover, the failure modes predicted by the method are also consistent with those observed experimentally, indicating that the method is able to reflect key physical aspects of connection response. The latter is especially important from the

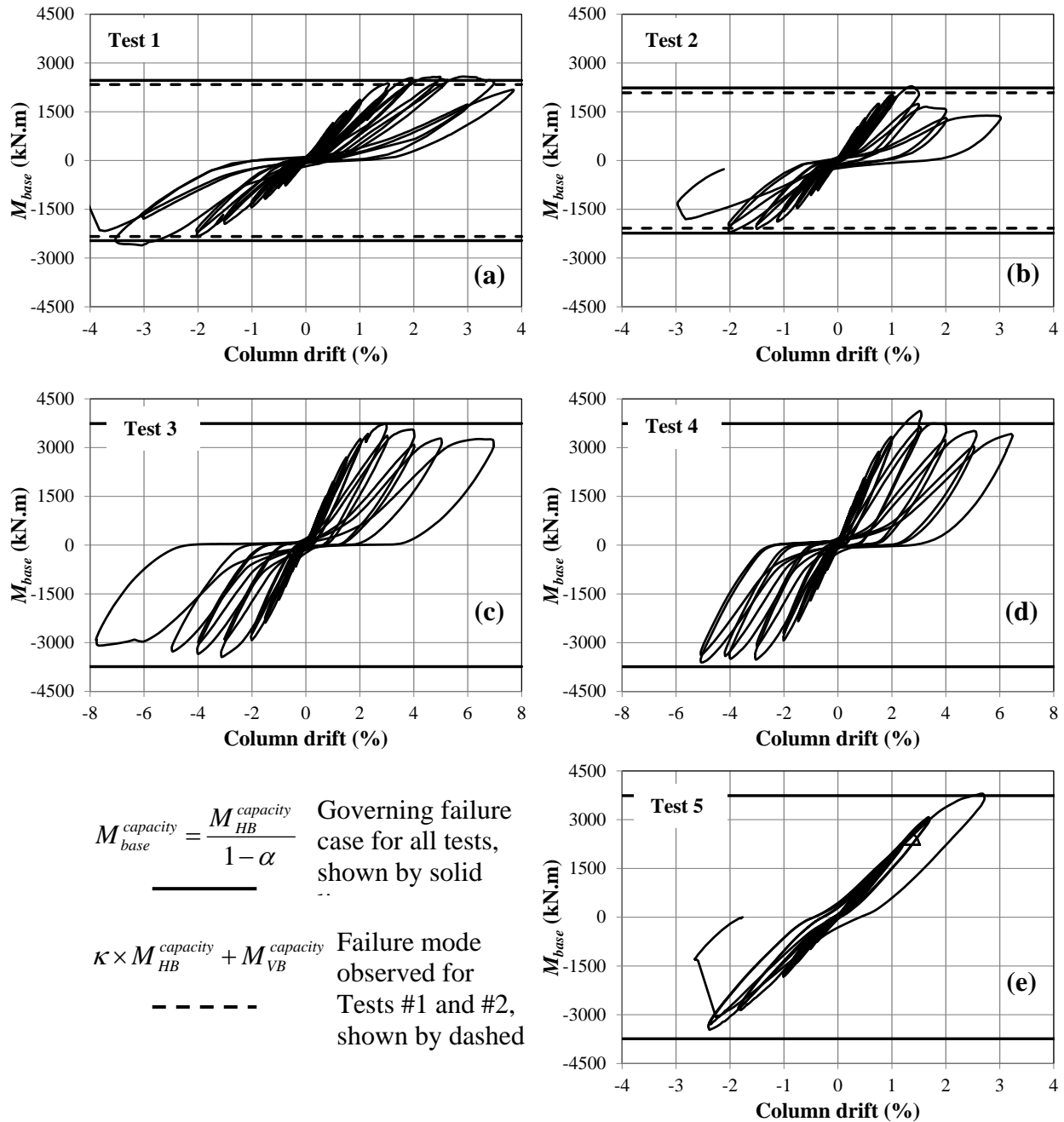perspective of generalizing the approach to connections configurations that are different from the ones tested.

Figure 17 – Load displacement curves with moment strengths estimated as per proposed method

Table 2 – Test results and comparison to strength model

Test #	Column Size, (b_f [mm])	P [kN]	d_{embed} [mm]	Base Plate, $t_p \times N \times B$ [mm]	z [m]	M_{base}^{max} [kN.m]	$d_{ref}^{\,*}$ [mm]	α	$\dfrac{M_{base}^{max}}{M_{base}^{capacity}}$ **
1	W14x370 (419)	445 (C)	508	$51 \times 762 \times 762$	2.84	2579(+)	920	0.45	1.05
						2613(-)			1.06
2	W18x311 (305)			$51 \times 864 \times 864$		2324(+)	978	0.48	1.04
						2168(-)			0.97
3		0	762	$51 \times 762 \times 762$	3.10	3741(+)	920	0.17	1.00
	W14x370 (419)					3444(-)			0.92
4		445 (C)				4124(+)	920	0.17	1.10
						3612(-)			0.97
5		667 (T)				3800(+)	920	0.17	1.02
						3464(-)			0.93
							Mean		1.01
							COV		0.06

*In all cases $d_{ref} > d_{embed}$, such that $d_{effective} = d_{embed}$.

**In all cases $M_{base}^{capacity} = M_{HB}^{capacity} /(1-\alpha)$.

DESIGN CONSIDERATIONS

It is anticipated that the method will be used iteratively in a design setting until the trial configuration (which is characterized by embedment depth, lower base plate dimensions) provides a strength $M_{base}^{capacity}$ that is sufficient to resist the applied moment (typically the moment capacity of the embedded column). The method was tested by applying it to several column sizes in the range of W14 to W33. In all cases, reasonable designs (embedment depths between 350-1000mm – depending on the moment capacity of the column, along with a base plate thickness of 50mm) were determined as per the method. An interesting observation was that for some column sections (heavy W14s, which had a high moment capacity but low depth), panel zone

shear was the critical mode of failure, i.e., $M_{base}^{capacity} = M_{HB}^{shear}/(1-\alpha)$. If these cases are encountered in practice, it may be expedient to increase M_{HB}^{shear} by providing reinforcement in the compression field region in the joint panel outside the column flanges. This was not considered in the experiments. In a majority of the cases (where joint shear did not govern), the dominant modes of failure were horizontal bearing (Equation 25), with or without breakout. Details of these design trials are provided in Grilli (2015).

SUMMARY, CONCLUSIONS, AND LIMITATIONS

This report presents findings from five tests representative of embedded column base (ECB) connections in mid- to high-rise steel moment frames, along with a strength characterization method based on experimental data and observed behavior. While these connections are common in current construction, their design is based on adaptations of guidelines for composite beam-column connections, or for coupling beams embedded in shear walls. Moreover, while they are assumed to be fixed connections, little evidence substantiates this assumption. Both of these knowledge gaps may be attributed to the lack of experimental data on ECB connections. The experiments described in this report, being the first of their kind, provide a direct assessment of the response of these connections, and the opportunity to develop design methods that reflect physical response peculiar to them. The main objective of these experiments is to examine the seismic response of these connections in three contexts: (1) to understand overall hysteretic response including failure modes, and deformation characteristics, (2) to support a strength characterization/design method, and (3) to examine whether ECB connections provide adequate rotational stiffness.

Experimental results

The experimental specimens were designed to represent current construction practice. All the specimens were cantilever columns loaded with cyclic lateral deformations under a constant axial load. The major test variables were the embedment depth, axial load (compressive, tensile, or zero), and the column cross-section. The experiments revealed that the base connections show hysteretic response with a high deformation capacity. In the initial stages of loading, damage was concentrated near the column flanges in the form of diagonal cracks. As loading progressed, crushing of concrete ahead of the compression flange resulted in nonlinearity in load displacement response. Diagonal shear cracks on the side of the joint were observed along with flexural cracks due to bending of the footing. Two types of failure were observed, one was associated with a gradual loss of strength owing to crushing of concrete in the compression zone ahead of the flange, whereas the other was characterized by uplift of a cone of concrete on the tension side of the connection. Based on these observations, three mechanisms for load resistance are postulated: (1) horizontal bearing of the column flanges against the concrete, (2) vertical bearing stresses on the embedded as well as stiffener plates, and (3) panel zone shear. Each of these mechanisms is further associated with one or more sub-mechanisms and local failure modes. An understanding of these mechanisms, sub-mechanisms, and their interactions is necessary for the development of a strength model. An analysis of the rotational stiffness of the ECB connections indicates that the connections may be flexible, such that first story drifts may be (on average) 25% larger than those estimated from a fixed base assumption.

In summary, the study indicates that if designed with consideration of both strength and stiffness, ECB connections are an attractive option for transferring large base moments and forces from

moment frame columns into the foundation. Moreover, they indicate excellent deformation capacity such that ≈2–3% drifts are reached in the experiments without significant loss of strength. A similar trend has been noted previously (Gomez *et al*., 2010; Kanvinde *et al*., 2013) for exposed base plate connections. In the context of current design practice, which typically requires the base connection to be stronger than the attached column (i.e., a capacity design), these observations suggest that utilizing the deformation and hysteretic characteristics of well-designed base connections may facilitate more economical design.

The general observations of this study must be interpreted within the context of its limitations, which are numerous. First, all the experiments examined only one generic detail, i.e., with the base plate at the lower end and the stiffener plate at the top. Other details may feature (1) a larger base plate at the top (2) supplemental anchor rods (3) additional stiffeners or haunches between the column and the base plate. Extrapolation of the method to these situations will require careful consideration of the physical distinctions between these and the tested configurations. Second, reinforcement in the footing was sparse by design, and the addition of reinforcement has the potential to affect the failure modes of horizontal bearing, panel zone shear, as well as vertical bearing (especially tension-side blowout). Third, extrapolating the observations to footing/embedment sizes that are significantly different from those tested is prone to error, since they are empirical and may be sensitive to size. In addition, the observed strengths as well as the failure modes may be sensitive to the manner of application of loading. Two issues are of importance here: (1) in the experiments, loading was applied in a non-proportional manner where the lateral loads were applied in the presence of a constant axial load, and (2) a constant moment-to-shear ratio was maintained throughout the tests. Seismic loads will, in general, not follow this

manner of load application. Finally, as discussed previously, the experiments address only the failure modes that occur in the immediate vicinity of the embedded connection; the boundary conditions of the experiments were designed to interrogate only these modes. Failure modes specific to foundation type (e.g., flexural failure in a grade beam or mat) are not addressed. To a large extent, the limitations above arise because the main objective of this study was to develop fundamental insights about the response of these connections. These insights may be refined and generalized through future experiments (e.g., on more connection types) and analytical research (e.g., finite element simulations) for more accurate and broader application. In any case, it is important to recognize that these limitations of the test program are inherited by strength characterization models that are based on these tests.

Strength characterization method

The strength characterization method developed in this report builds on the experimental observations that in ECB connections, the applied moment and axial load are resisted three primary mechanisms: (1) horizontal bearing of the column flanges against the concrete, (2) vertical bearing stresses on the embedded as well as stiffener plates, and (3) panel zone shear. These mechanisms are interactive, and each is associated with one more failure modes. The method characterizes the strengths associated with each of these failure modes, and establishes the nature of interactions between these mechanisms such that strengths associated with the individual failure modes may be suitably combined to characterize overall connection strength.

The proposed method seeks to balance four considerations: (1) reliance on published models and fundamental physics/mechanics to characterize interactions and failure modes, (2) minimization

of ad-hoc, calibrated factors, (3) agreement with test data in terms of strengths as well as qualitative failure modes, (4) convenience of application within a practical or design setting. The empirical (or calibrate d) aspects of the method include: (1) the relationship for $d_{effective}$, which characterizes the attenuation of stresses through the depth of the footing, (2) the approach to characterize the distribution of moment between the horizontal and vertical bearing mechanisms, i.e., the α factor, (3) the approach to quantify the degradation of the horizontal bearing strength after it has achieved its peak, through the κ factor, and (4) the modification factor η to account for the effect of stress gradient on concrete breakout. While calibrated empirically, these have basis in classical derivation (in the first case), and physical observations of test response (in the three latter cases).

The method assumes that all dimensions and material properties of all components of the connection are known or specified. In addition, the method also assumes that the axial force is given. It is anticipated that this method will be used iteratively to size various parts of the footing given the loading and other (dimensional, architectural, planning) constraints. Since the method identifies the type of failure controlling the moment capacity (and the moment capacities with other response modes), it explicitly provides guidance for optimal re-sizing and iteration. While the method can be applied through hand-analysis or a spreadsheet, a computer program is most convenient for its implementation. The method is tested to design connections for several column sizes, and in general, is determined to provide reasonable designs (in terms of embedment and base plate dimensions).

The proposed method has several limitations, which must be considered in its interpretation and application. As mentioned previously, is important to note that the limitations of the experimental program are inherited by the method as well. While the main purpose of the method is to enable extrapolation beyond the conditions tested, it is prudent to recognize that the empirical aspects of the method may not be generally applicable. In fact, extrapolating the method to footing/embedment sizes that are significantly different from the method is prone to error, since the empirical aspects of the method may be sensitive to size. Where available, methods that are based on similarly sized (or detailed) connections may be used. For example, the methods developed by Cui *et al*. (2009), or by Barnwell (2015), may be more suitable for shallowly embedded connections with $d_{embed} \leq$ 200mm. On the other hand, where such approaches are not available, aspects of the presented method may be leveraged or modified where possible. For example, the effect of anchor rods (if provided on the lower base plate) may be readily incorporated by modifying the vertical bearing limit states by adding the anchor rod strength in the calculation of M_{VB}^{t}. Moreover, as discussed previously, the method (like the experiments) only addresses failure modes that occur in the immediate vicinity of the embedded connection; and not those triggered by overall foundation failure. These are presumably sensitive to foundation type. To overcome some of these limitations, future work may involve additional experiments on varied details, and finite element simulations for more accurate understanding of internal force transfer. Finally, the method provides deterministic estimates of nominal strength. Appropriate $\phi-$ factors are required to ensure adequate margins of safety against failure; these may be developed through reliability analysis.

NOTATIONS

α	Fraction applied moment resisted by vertical bearing mechanism
A_{35}	Projected area of a concrete 35 degree failure cone emanating from the edges of concrete stress block
$B, N \ t_{plate}$	Base plate dimensions: Width, length (in direction of load), thickness
β, β_1	Factors to account for concrete confinement and effectiveness in bearing
$\beta_{base}, \beta_{base}^{test}$	Rotational stiffness of base connection: generic, experimental
b_f, t_f	Width, thickness of column flange
β_{frame}	Rotational stiffness of framing members at top of column
b_j, b_o	Effective joint width, outer joint panel zone width
d, d_w	Column depth, web depth
d_{cover}	Thickness of concrete that must be ruptured for breakout
$d_{embed}, d_{effective}$	Embedment depth, effective embedment depth
d_{ref}	Depth at which horizontal bearing stresses attenuate to zero
d_L	Depth of lower horizontal concrete bearing stress block
d_U	Depth of upper horizontal concrete bearing stress block
d_v	Length of vertical bearing zone on base plate
Δ_{base}^{max}	Drift corresponding to M_{base}^{max}
Δ_{base}^{y}	Drift corresponding to M_{base}^{y}
$\Delta_{fixed}, \Delta_{test}$	Calculated drift of column due to a unit load applied at the top of the column – assuming a fixed base, experimental value

E_{steel}, $E_{concrete}$ Moduli of elasticity of steel and concrete

$F_{breakout}^{t,c}$ Force at which breakout occurs, on tension or compression side

f_c' Compressive strength of concrete

F_{flange}^{top}, F_{flange}^{bottom} Forces in column flanges at the top and bottom of embedment zone

F_y Minimum specified yield strength of steel

F_y^{column}, F_y^{plate} Minimum specified yield stress of column and base plate

f_{VB}^{b} Vertical bearing stress on base plate

f_{VB}^{M}, f_{VB}^{P} Vertical bearing stress on base plate due to moment, axial load

h Distance between the centerline of column flanges

I_{beam}, I_{column} Moment of inertia of notional beam, column

κ Degradation factor for horizontal bearing

L_{beam} Length of notional beam framing into top of column

M_{base}, M_{base}^{max}, M_{base}^{y} Column base moment – generic, maximum in test, yield

$M_{base}^{capacity}$ Base moment capacity

M_{HB}, $M_{HB}^{capacity}$ Moment resisted through horizontal bearing stresses

$M_{HB}^{bearing}$, M_{HB}^{shear} Moment capacity of provided by horizontal bearing, shear

M_p Plastic moment capacity of column

M_{VB}, $M_{VB}^{capacity}$ Moment resisted through vertical bearing mechanism, capacity

M_{VB}^{b} Moment capacity of vertical bearing mechanism due to concrete crushing

M_{VB}^{c}	Moment capacity of vertical bearing mechanism due to concrete breakout under the compression toe of the base plate
M_{VB}^{t}	Moment capacity of vertical bearing mechanism due to concrete breakout under the compression toe of the base plate
M_{VB}^{y}	Moment capacity of vertical bearing mechanism due to yielding of base plate on tension or compression side
n	Length of flap of the base plate in the direction of loading
η	Factor used in concrete breakout equation accounting for differences in loading conditions implied by CCD method and ECB connections
P	Column axial load
$\theta_{drift}, \theta_{base}, \theta_{footing}$	Column drift angle, base rotation, footing rotation
V_{j}	Vertical shear force in the joint panel
V_{column}	Imposed column shear
$V_{steel}, V_{strut,inner}, V_{strut,outer}$	Shear capacity of steel web, concrete strut, outer panel
z	Height of load application above concrete surface

REFERENCES

AISC. (2010). *Seismic Provisions for Structural Steel Buildings (ANSI,AISC 341-10)*, American Institute of Steel Construction, Inc., Chicago, IL.

ASCE Guidelines (1994). "Guidelines for Design of Joints Between Steel Beams and Reinforced Concrete Columns," *Journal of Structural Division*, ASCE, Vol. 120(8), pp. 2330-2357.

ASCE Task Committee (1998). "Design Guide for Partially Restrained Composite Connections," *Journal of Structural Engineering*, ASCE, Vol.124 No. 10, pp.1099-1114.

Astaneh, A., Bergsma, G., and Shen J.H. (1992). "Behavior and Design of Base Plates for Gravity, Wind and Seismic Loads," *Proceedings of the National Steel Construction Conference*, Las Vegas, Nevada, AISC, Chicago, IL.

Barnwell, N. (2015). "Experimental Testing of Shallow Embedded Connections Between Steel Columns and Concrete Footings," Masters Thesis, Brigham Young University.

Bažant, Z.P. (1984). "Size Effect in Blunt Fracture: Concrete, Rock, Metal," Journal of Engineering Mechanics, ASCE, 110(4), 518–535.

Becker, J., Bevis, M. (2004). "Love's Problem", *Geophys. J. Int.*, 156, 171 - 178.

Bjorhovde, R., Brozzetti, J., Colson, A. (1988). *Connections in Steel Structures: Behaviour, Strength, and Design*. New York: Elsevier Science Pub. Co. Print.

Bruneau, M., Uang, C., Whittaker, A. (1997). *Ductile Design of Steel Structures*. New York: McGraw-Hill Professional; 1 edition (October 1, 1997). Print.

Burda, J.J., and Itani, A.M. (1999). "Studies of Seismic Behavior of Steel Base Plates," *Report No. CCEER 99-7*, Center of Civil Engineering Earthquake Research, Department of Civil and Environmental Engineering, University of Nevada, NV.

Cordova, P.P. and Deierlein, G.G. (2005). "Validation of the Seismic Performance of Composite RCS Frames: Full-Scale Testing, Analytical Modeling, and Seismic Design," Technical Report 154, Blume Earthquake Engineering Center.

Cui, Y., Nagae, T., Nakashima, M. (2009). "Hysteretic Behavior and Strength Capacity of Shallowly Embedded Steel Column Bases." *Journal of Structural Engineering,* ASCE Vol. 135, No. 10, October 2009, pp. 1231-1238.

Deierlein, G.G., Sheikh, T.M., Yura, J.A., and Jirsa, J.O. (1989). "Beam-Column Moment Connections for Composite Frames: Part 2," *Journal of Structural Engineering* ASCE, Vol. 115, November 1989, pp.2877-2869.

DeWolf J.T., and Sarisley, E.F. (1980). "Column Base Plates with Axial Loads and Moments," *Journal of the Structural Division*, ASCE, Vol. 106, No. 11, November 1980, pp. 2167-2184.

Fahmy, M., Stojadinovic, B., and Goel, S.C. (1999). "Analytical and Experimental Studies on the Seismic Response of Steel Column Bases," *Proceedings*, 8th Canadian Conference on Earthquake Engineering, Vancouver, Canada.

Fisher, J.M. and Kloiber, L.A. (2006), "Base Plate and Anchor Rod Design," 2nd Ed., Steel Design Guide Series No. 1, American Institute of Steel Construction, Inc., Chicago, IL.

Fuchs, W., Eligehausen, R. and Breen, J.E. (1995). "Concrete Capacity Design (CCD) Approach for Fastening to Concrete," *ACI Structural Journal,* Vol. 92, No. 1, pp. 73–94.

Gomez I.R., Kanvinde A.M. and Deierlein G.G. (2010). "Exposed Column Base Connections Subjected to Axial Compression and Flexure," *Report Submitted to the American Institute of Steel Construction (AISC)*, Chicago, IL.

Gomez, I.R., Kanvinde, A.M., Smith, C.M., and Deierlein, G.G., (2009), "Shear Transfer in Exposed Column Base Plates," Report Submitted to the American Institute of Steel Construction, Chicago, IL.

Grilli, D.A. (2015). "Seismic response of embedded column base connections and anchorages," Doctoral Dissertation, University of California, Davis, CA 95616.

Grilli, D.A., and Kanvinde, A.M. (2013). "Special Moment Frame Base Connection: Design Example 8," 2012 IBC SEAOC Structural/Seismic Design Manual, Volume 4, Examples for Steel-Frame Buildings, 255-280.

Hetenyi, M. (1946). Beams on Elastic Foundation: Theory with Applications in the Fields of Civil and Mechanical Engineering. University of Michigan Press (August 1, 1946). Print.

Hutchinson, T.C., Chai, Y.H., and Boulanger, R.W. (2005). "Simulation of Full-Scale Cyclic Lateral Load Tests on Piles," Journal of Geotechnical and Geoenvironmental Engineering, ASCE, Vol. 131, No. 9, pp. 1172-1175.

Kanvinde, A.M., Jordan, S.J., and Cooke, R.J. (2013). "Exposed Column Baseplate Connections in Moment Frames – Simulations and Behavioral Insights," Journal of Constructional Steel Research, Elsevier, 84, 82-93.

Kanvinde, A.M., Grilli, D.A., and Zareian, F. (2012). "Rotational Stiffness of Exposed Column Base Connections – Experiments and Analytical Models," Journal of Structural Engineering, ASCE, 138(5), 549-560.

Krawinkler, H., Gupta, A., Medina, R., and Luco, N. (2000), "Loading Histories for Seismic Performance Testing of SMRF Components and Assemblies," SAC Joint Venture, Report no. SAC/BD-00/10. Richmond, CA.

Krawinkler, H., Parisi, F., Ibarra, L., Ayoub, A., and Medina, R., (2000). "Development of a Testing Protocol for Woodframe Structures," CUREE Publication No. W-02.

Marcakis, K. and Mitchell, D. (1980) "Precast Concrete Connections with Embedded Steel Members," Prestressed Concrete Institute Journal, V. 25, No. 4, July/Aug. 1980, pp. 88-116.

Mattock A. H. and Gaafar G. H. (1981). "Strength of Embedded Steel Sections as Brackets," ACI Journal, Vol. 79, No. 2.

Morino, S., Kawaguchi, J., Tsuji, A., and Kadoya, H. (2003). "Strength and Stiffness of CFT Semi-embedded Type Column Base," *Proceedings of ASSCCA 2003 Conference,* Sydney, Australia, A. A. Balkema, Sydney, Australia.

Motter, C.J., (2015). *Large-scale Testing of Steel-reinforced Concrete (SRC) Coupling Beams Embedded into Reinforced Concrete Structural Walls.* Dissertation, University of California, Los Angeles. Ann Arbor: ProQuest/UMI, 2014. (Publication No. 3629336).

Myers, A.T., Kanvinde, A.M., Deierlein, G.G., and Fell B.V. (2009). "Effect of Weld Details on the Ductility of Steel Column Baseplate Connections," *Journal of Constructional Steel Research*, Elsevier, Vol. 65, No. 6, June 2009, pp. 1366-1373.

Pertold J., Xiao, R. Y., and Wald, F. (2000a). "Embedded Steel Column Bases – I. Experiments and Numerical Simulation," *Journal of Constructional Steel Research*, Vol. 56, pp. 253-270.

Pertold, J., Xiao, R. Y., and Wald, F. (2000b). "Embedded Steel Column Bases – II. Design Model Proposal," *Journal of Constructional Steel Research*, Vol. 56, pp. 271-286.

Shahrooz, B. M., Remetter, M. E., and Qin, F. (1993), "Seismic Design and Performance of Composite Coupled Walls," Journal of Structural Engineering, ASCE, Vol. 119, No. 11,

pp. 3291–3309, Reston, VA.

Sheikh, T.M., Deierlein, G.G., Yura, J.A., and Jirsa, J.O. (1989). "Beam-Column Moment Connections for Composite Frames: Part 1," *Journal of Structural Engineering* ASCE, Vol. 115, November 1989, pp. 2858-2876.

Thambiratnam, D.P., and Paramasivam, P. (1986). "Base Plates Under Axial Loads and Moments," *Journal of Structural Engineering*, ASCE, Vol. 112, No. 5, May 1986, pp. 1166-1181.

Tremblay, R., Timler, P., Bruneau, M., and Filiatrault, A., (1995). "Performance of Steel Structures During the 1994 Northridge Earthquake," *Canadian Journal of Civil Engineering*, Vol. 22, pp. 338-360.

Zareian, F., and Kanvinde, A.M. (2013). "Effect of Column Base Flexibility on the Seismic Safety of Steel Moment Resisting Frames," Earthquake Spectra, Earthquake Engineering Research Institute, 29(4), 1-23.

APPENDIX

LISTING OF PROGRAM TO CALCULATE MOMENT STRENGTH OF EMBEDDED CONNECTIONS

AS PER THE PROPOSED METHOD

```matlab
function[Mcap] = Mbase_predict(P,dembed,section,z,N,B,tp,W,fc,Fy)

%READ ME================================================================
%Function implements a strength prediction method to calculate the
%maximum base moment for an embedded column base connection

%INPUTS:
%axial load, embedment depth, column dimensions, base plate dimensions,
%and steel and concrete material

%definitions
%   P:      axial load, compressive (+), tensile (-)  [kips]
%   dembed: embedment depth [in]
%   section: [string] Embedded column section (must use section.m, or recode
to
%            define column dimensions manually
%   z:      height of horizontal load application (moment/shear ratio) [in]
%   N:      length of base plate (in loading direction) [in]
%   B:      width of base plate [in]
%   tp:     thickness of base plate [in]
%   W:      width of foundation (perpindicular to loading direction) [in]
%   fc:     compressive strength of concrete [ksi]
%   Fy:     yield strength of base plate [ksi]

%OUTPUTS:
% Base moment capacity [k-ft]

%definitions
%   Mt_vb:  moment due to vertical bearing at breakout on tension side
%   Mb_vb:  moment due to vertical bearing at bearing failure
%   My_vb:  moment due to vertical bearing at base plate yield
%   Mbearing_b: moment due to horizontal bearing at bearing failure
%   Mh_ps:  moment due to horizontal bearing at panel shear failure
%   Mcap_h: maximum moment due to horizontal bearing
%   Mcap_v: maximum moment due to vertical bearing
%   Mcap:   maximum moment

%supplimentary information printed to command window
%========================================================================

format shortG
close all;

numpts = 1.0e5;
M = linspace(1.0e2,1.0e6,numpts);   %moment increments

%column section properties
[~,d,tw,bf,tf,Iz,~,~,~,~,~,~,~,~] = wsection(section);

%constants
V = M./z;                  %constant moment-to-shear ratio
Mpa = 6.89475908677537; %ksi to Mpa conversion
ki = 1.7;                  %inner panel strength factor set to 1.7
ko = 1.25;                 %outer panel strength factor set to 1.25
```

```
bi = bf;                    %inner joint width
bo = (B - bf)/2;            %outer joint width
bj = bi + bo;               %effective joint width
dj = d - tf;
Es = 29000;                 %elastic modulus steel
Ec = 3605;                  %elastic modulus concrete


%concrete bearing factor
beta1 = 0.85;
if fc >= 4.5; beta1 = 0.80; end;
if fc >= 5.0; beta1 = 0.75; end;
if fc >= 5.5; beta1 = 0.70; end;
if fc >= 6.0; beta1 = 0.65; end; %ACI 318 (R10.2.7)


%parameters
gamma = beta1.*2.0;   %concrete bearing capacity enhancement due to
                      %confinment effects
beta = 0.6;           %maximum fraction of neutral axis depth that
                      %horizontal bearing depth can attain
dv = 0.3.*N;          %fraction of N that contributes to vertical bearing
mu = 2;               %calibrated parameter to adjust kappa
nu = 1.5;             %calibrated parameter to adjust breakout capacity
C = 1.77;            %calibrated parameter to adjust dref


%failure flags
hb_flag = 0;
ps_flag = 0;



%calculated constants
n = 1/2*(N - d); %flap length

%determine dref and alpha==================================================

betaref = (Ec/(4*Es*Iz))^(1/4);
dref = C/betaref;                %reference depth
if dembed > dref,
    dembed = dref;
end

alpha = 1 - dembed/dref;  %alpha assumed linear function of dembed

%RESPONSE==================================================================

for j = 1:numpts

%horizontal moment response===============================================

%horizontal bearing

Vbar = V(j)./(gamma.*fc.*bj);

dR = (1/2).*(Vbar + dembed - sqrt(dembed.^2 - 2.*dembed.*Vbar -...
      Vbar.^2 - 4.*Vbar.*z + 4.*alpha.*Vbar.*z));
```

```matlab
dL = dR - Vbar;

Mbearing_hb_test = M(j).*(1 - alpha);
Mbearing_max = (-dembed - 2.*z + 2.*alpha.*z +...
    1./2.*sqrt(-4*(-2*beta*dembed^2 + beta^2*dembed^2) +...
    (2*dembed + 4*z - 4*alpha*z)^2)).*z.*gamma.*fc.*bj.*(1 - alpha);

if hb_flag == 0
    if Mbearing_hb_test > Mbearing_max
        hb_flag = 1;
        Mbearing_hb = M(j).*(1 - alpha);
    end
end

%inner panel

if ps_flag == 0
    if Mbearing_hb_test > Mbearing_max
        Mshear_hb = inf;  %if shear failure not achieved when dR = dRmax,
                          %panel shear capacity set to infinite
        ps_flag = 1;
    end
end

Vspn = 0.6*Fy*tw*(dembed - (dR + dL)/2);    %strength of steel web panel

Vicn = min(ki*sqrt(fc*Mpa)*bi*(dembed ...
        - (dR + dL)/2)./Mpa,0.5*fc*bf*dj);  %strength of inner strut

Von = ko.*sqrt(fc*Mpa)./Mpa.*bo.*(dembed -...
        (dR + dL)/2);                       %strength of outer strut

M_ps = (Vspn*(d - 2*tf) + Vicn*dj + 1.25*Von*dj);

if ps_flag == 0
    if M_ps <= Mbearing_hb_test
        ps_flag = 1;
        Mshear_hb = M(j)*(1 - alpha);
    end
end
%=========================================================================
end

%vertical moment response=================================================
if P >= 0
    alphaP = 1.0;  %fraction of P transferred to the base, compression
elseif P < 0
    alphaP = 1.0;  %fraction of P transferred to the base, tension
end

%bearing failure check
Mb_vb = (1.7*fc - alphaP*P/(B*N))*(N - dv)*B*dv;
```

```matlab
%base plate yield check

My_vb = (tp^2*Fy/(2*n^2) - alphaP*P/(B*N))*(N - dv)*B*dv;

%breakout check

%CCD

Anc = min(W*(dv + 3.*dembed),(dv + 3.*dembed)*(B + 3.*dembed));
                                %breakout area
                                %adjusted only if width of block interferes
                                %with breakout cone

Qc = (1./sqrt(dembed).*(40./9).*sqrt(fc.*1000)./1000.*Anc).*nu;

Mt_vb = (Qc + alphaP*P*dv/N)*(N - dv);

% end

%NOTE: no check for downward bearing in code

%failure mode combinations ================================================

[Mcap_v,indv] = min([Mb_vb,My_vb,Mt_vb]);
[Mcap_h,indh] = min([Mbearing_hb,Mshear_hb]);
kappa = nan;

if Mcap_v/alpha <= Mcap_h/(1 - alpha)
    cse = 1;
    [Mcap,ind] = min([Mt_vb/alpha, Mcap_h + Mb_vb, Mcap_h + My_vb]);
else
    cse = 2;
    kappa = ((Mcap_v*(1 - alpha))/(Mcap_h*alpha)).^(-mu);
    if Mbearing_hb < Mshear_hb
    [Mcap,ind] = max([kappa.*Mcap_h + Mcap_v, Mcap_h./(1 - alpha)]);
    else
        Mcap = Mcap_h/(1 - alpha);
        ind = 3;
    end
end

%print out=================================================================

if indv == 1
    vcontrol = 'Vertical bearing';
elseif indv == 2
    vcontrol = 'Base plate yield';
elseif indv == 3
    vcontrol = 'Breakout';
end

if indh == 1
    hcontrol = 'Horizontal bearing';
elseif indh == 2
```

```matlab
        hcontrol = 'Panel shear';
end

if cse == 1
    if ind == 1
        maxcond = 'Breakout only';
    elseif ind == 2
        maxcond = 'Vertical bearing, horizontal';
    elseif ind == 3
        maxcond = 'Base plate yield, horizontal';
    end

elseif cse == 2
    if ind == 1
        maxcond = 'Degraded horizontal bearing, vertical';
    elseif ind == 2
        maxcond = 'Horizontal bearing at maximum';
    elseif ind == 3
        maxcond = 'Panel shear only';
    end

end

%print information to command window
fprintf('PARAMETERS: %g\n','')
fprintf(' %g\n','')
fprintf('alpha: %g\n',alpha)
fprintf('kappa: %g\n',kappa)
fprintf('gamma: %g\n',gamma)
fprintf('beta: %g\n',beta)
fprintf('dembed: %g\n',dembed)
fprintf('dreference: %g\n',dref)
fprintf(' %g\n','')
fprintf('CONTROL AND MAXIMUM CONDITION: %g\n','')
fprintf(' %g\n','')
fprintf('Case: %g\n',cse)
fprintf('Horizontal control: %s\n',hcontrol)
fprintf('Vertical control: %s\n',vcontrol)
fprintf('Maximum condition: %s\n',maxcond)
fprintf(' %g\n','')
fprintf('VALUES: %g\n','')
fprintf(' %g\n','')
fprintf('Mh_b: %g\n',Mbearing_hb./12)
fprintf('Mh_ps: %g\n',Mshear_hb./12)
fprintf('Mv_bpyield: %g\n',My_vb./12)
fprintf('Mv_tbreak: %g\n',Mt_vb./12)
fprintf('Mh %g\n',Mcap_h./12)
fprintf('Mv %g\n',Mcap_v./12)
fprintf(' %g\n','')
fprintf('Mcap %g\n',Mcap./12)
fprintf(' %g\n','')
Mcap = Mcap./12;
```